

Do Nonorthogonally and Irregularly Sampled Scalar Velocities Contain Sufficient Information to Reconstruct an Orthogonal Vector Current Field?

HYUN SUP SOH AND SUNG YONG KIM

*Environmental Fluid Mechanics Laboratory, Department of Mechanical Engineering,
Korea Advanced Institute of Science and Technology, Yuseong-gu, Daejeon, South Korea*

P. MICHAEL KOSRO AND ALEXANDER L. KURAPOV

College of Earth, Ocean, and Atmospheric Sciences, Oregon State University, Corvallis, Oregon

(Manuscript received 31 March 2017, in final form 28 November 2017)

ABSTRACT

This paper addresses how well a two-dimensional orthogonal vector current field can be reconstructed from a set of nonorthogonally and irregularly sampled scalar velocity data. High-frequency radar (HFR)-derived surface radial scalar velocities are sampled on a polar or elliptical coordinate grid as a directional projection of two-dimensional vector currents for a viewing angle of the individual HFRs. Synthetic radial velocity maps are generated by sampling two-dimensional surface vector currents obtained from a simple spectral model and a realistic regional circulation model on the polar or elliptical grid points configured similarly as the operational HFRs. Then, the sampled radial velocity maps are combined into a vector current field using inverse methods: least squares fitting and optimal interpolation. In this paper, uncertainty and misfit are defined as the degrees of insufficiency to resolve the vector current and the difference between the true and estimated vector currents, respectively. The uncertainty and misfit are evaluated in terms of several simulation parameters built into the simple spectral model and the degrees of the quality and the observational error of the radial velocity maps associated with the simulated missing data and noise level, respectively. A greater number of missing data and higher observational errors correspond to an increase in the standard deviation of the misfit and a significant reduction in the effective spatial coverage of the vector current fields. This paper provides technical details for resolving a vector current field and guidelines for the practical design of the spatial sampling of the current field using the HFRs.

1. Introduction

Observational instruments used for oceanographic sampling are technically unique, which can affect the way to grid the sampled data and to estimate the corresponding errors. For example, satellite altimeters report sea surface heights (SSHs) along a repeat-orbit path that covers the entire globe within a period of less than 10 days. Gridded SSHs and geostrophic currents are obtained from the along-track SSHs using objective mapping in time and space (e.g., [Leben et al. 2002](#); [Le Traon et al. 1998](#); [Ducet et al. 2000](#); [Wilkin et al. 2002](#)). A shore-based high-frequency radar (HFR), via the interpretation of Bragg-backscattered radar signals, reports a time-averaged radial velocity map with $O(1-10)$ -km spatial spacing in a polar coordinate grid

for the monostatic configuration or in an elliptical coordinate grid for the bistatic and multistatic configurations, which consist of the current components that are projected onto a radar bearing angle. Thus, a single two-dimensional vector solution requires the radial velocities from at least two radars (e.g., [Crombie 1955](#); [Barrick et al. 1977](#); [Lipa and Barrick 1983](#); [Paduan and Graber 1997](#); [Kim et al. 2008](#); see [appendix A](#)).

In ocean sensing instruments, the observational error is a combination of the sampling error, measurement error, mapping error, and systematic error. The sampling error, which is related to finite sampling or the subsampling of a continuous and whole field, is defined as the difference between the true value and the sampled data in a view of how well the sampled field represents the true field (e.g., [Bendat and Piersol 2000](#); [Stewart 2006](#)). The measurement error is associated with the inaccurate treatment of selected samples and

Corresponding author: Sung Yong Kim, syongkim@kaist.ac.kr

DOI: 10.1175/JTECH-D-17-0062.1

© 2018 American Meteorological Society. For information regarding reuse of this content and general copyright information, consult the [AMS Copyright Policy](#) (www.ametsoc.org/PUBSReuseLicenses).

depends on the sensors. The mapping error represents the difference between the true and gridded data associated with the spatial and temporal smoothing (e.g., Bretherton et al. 1976; Wunsch 1996; Emery and Thomson 1997). Geometric dilution of precision [GDOP; see section 3c(1) for more details] can be an example of the systematic error because the GDOP characterizes the intrinsic limitations of an observational system resulting from the geographical constellation or spatial configuration of individual subsystems when the observational system is composed of individual subsystems (e.g., Pierce et al. 1948; Wells et al. 1986; Prandle 1991; Chelton and Schlax 1994; Chapman et al. 1997; Greenslade et al. 1997; Levanon 2000). However, these elements of the observational error are not independent or clearly separable in certain cases depending on the instruments.

For example, errors in the surface current measurements using the HFRs can be described by 1) the observational error of the radial velocities and 2) the uncertainty (ν or κ ; see section 2c for more details) of the vector currents caused by mapping of the radial velocities into a vector current. First, the observational error of the radial velocities includes the sampling error and measurement error of the radial velocities, which may not be clearly differentiated in the observed radial velocities because both errors are reported as a single term as part of the time-averaged discrete radial velocity at the ocean surface. However, when the surface radial velocities are sampled from the idealized and numerical model outputs, the measurement error caused by malfunctions of the instrument can be eliminated and the sampling error can be identified. The sampling error is related to how well the sampled data at finite spatial and temporal resolutions represent the true field because the observed radial velocity is a spatially averaged value within individual polar or elliptical coordinate patches, wherein areas increase with a greater range from the radar site (e.g., Kim et al. 2008). Second, the uncertainty (ν or κ) of the vector currents are associated with the mapping error and systematic error. For example, in the extraction of a single two-dimensional vector solution from the multiple radial velocities using optimal interpolation (OI), the error covariance indicates the covariance of the mapping error, which is implemented with the observational error of the radial velocities [see Eqs. (1) and (13)]. In addition, as part of the systematic error, the GDOP results from the spatial arrangement of the individual HFRs contributing radial velocity data to the vector current map (e.g., Chapman et al. 1997; Levanon 2000). Thus, the GDOP can be defined as the uncertainty of the least squares fit (LSF)-mapped vector currents and

smear in the uncertainty of the OI-mapped vector currents as partial information (e.g., Kim et al. 2008).

Deriving the orthogonal vector components from the nonorthogonally and irregularly sampled velocity data has been a difficult problem in oceanographic data analyses as a result of the increased error in certain geometries (e.g., O'Keefe 2005; Yoo et al. 2017; Cosoli and Bolzon 2015). Note that *nonorthogonally* means that the orthogonal projections of the vector are not available, and *irregularly* means that the sample spacing is irregular and the independent vector projections are not available at the same point. The errors of the geostrophic velocities that were estimated from the satellite along-track SSHs were evaluated using a spectral analysis of the high-resolution ocean circulation model outputs (Leeuwenburgh and Stammer 2002). The significant spatial and temporal inhomogeneity in the mapping error may generate unrealistic and spurious oceanographic features (Chelton and Schlax 2003; Schlax and Chelton 2003). Kim et al. (2008) reported the mathematical relevance and performance of the two inverse methods (LSF and OI) in extracting a vector current map from the HFR-derived radial velocity maps. Additionally, Yoo et al. (2017) focused on the covariance estimates of the orthogonal vector currents directly from the HFR-derived radial velocities without any redundant steps, which aligns with the estimate of the kinematic and dynamic quantities directly from the radial velocity maps addressed elsewhere (e.g., Kim 2010).

The primary objectives of this work are to 1) determine whether imperfect, nonorthogonal, and spatially separated scalar velocity data contain sufficient information to reconstruct a vector current field and 2) investigate the influence of the missing data and the observational error of the radial velocities, which can be differentiated from the other technical studies mentioned above (e.g., Kim et al. 2008; Kim 2010; Yoo et al. 2017). In the early stage of the use of HFR-derived surface currents in scientific research, there were inconsistent current measurements compared with other in situ current observations [e.g., the Coastal Ocean Dynamics Experiment (CODE) in the 1980s]. Along with recent technical developments, the capability and feasibility of the HFRs have been improved up to the level that the HFR-derived surface currents capture well the responses to the geophysical forces (e.g., tides, winds, and low-frequency forcing) (e.g., Chavanne et al. 2007; Kim et al. 2011; Paduan and Washburn 2013; Kirincich 2016). However, whether the scalar radial velocity maps sampled from the HFRs contain sufficient information to reconstruct the real signals has not been evaluated, which was not discussed in Kim et al. (2008) because they focused on several aspects of the chosen inverse methods and their performance. In addition, the

uncertainty of the vector currents was not clearly defined. For instance, it was not discussed how the observational error of the radial velocities is propagated and implemented in the vector current estimates.

To these ends, we obtain the true vector current fields from the model outputs (e.g., simple spectral and realistic numerical models); sample them as the radial velocity maps; combine the radial velocity maps into the vector current maps; and, finally, compare the true and estimated vector current fields. To better evaluate the performance of the reconstruction, the missing data and the observational error in the radial velocities are additionally simulated in the sampled radial velocity maps (see [section 2b](#)). As a metric to evaluate whether the sampled radial velocity maps contain sufficient information for reconstructing the vector currents, we propose the (spatially averaged or individual) ensemble-averaged misfit between the true and estimated currents [Eqs. (23) and (25)]. This work can be complementary to what [O’Keefe \(2005\)](#) and [Cosoli and Bolzon \(2015\)](#) conducted in the vector current extraction using LSF in terms of the radar geometry, flow patterns, and various error sources. Note that the subgrid-scale processes are not included in this work (e.g., mapping errors that arise from using a single value to represent the varying velocity over a single cell).

As minor notes, the grid from which the radial velocities are sampled is referred to as the polar coordinate in the following section based on the monostatic configuration. Additionally, the technique proposed in this paper is applicable to a phased-array radar system using beam forming [e.g., Wellen Radar (WERA) systems] with limitations because some of the phased-array systems sample the radial velocities directly onto a Cartesian grid. In others cases, the radial velocities derived from the phased-array radars have been reported on the polar or elliptical coordinate grid for further generic applications, such as data assimilation with numerical models (e.g., the WERA system at the University of Hawaii) and the quality assurance and quality control (QAQC) of the radial velocities (e.g., [Yoo et al. 2017](#)).

The remainder of this paper consists of four sections. In [section 2](#) we describe the simulations used to extract a vector current field from two radial velocity maps obtained from the simple spectral model and to evaluate the uncertainty in terms of the simulation parameters in the model. In [section 3](#) we explain basic information regarding the sampling of the radial velocities from the true vector current fields obtained from realistic numerical simulations, and then we evaluate the estimated and true vector current fields with the data quality of the radial velocity maps and the degrees of the observational errors. In [sections 4](#) and [5](#) we discuss the results and present our conclusions, respectively.

2. Idealized simple spectral model

a. True vector currents

In this section the true vector current fields are obtained from 1) an analytic solution that represents uniform, horizontal shear, or (Rankine) vortical flow patterns (e.g., [Kundu and Cohen 2002](#)); and 2) a spectral model that is defined by either a wavenumber-domain energy spectrum or a physical-domain covariance function (see [appendix A](#) for more details). Although the spectral model can be formulated to include variance in both the wavenumber and frequency domains [see [Yoo et al. \(2017\)](#) for more details], in this paper each true vector current field is generated independently in time. Examples of the true vector current fields having horizontal shear and vortical flow patterns sampled on a 1-km spatial resolution grid ($\Delta l = 1$ km) are presented as black arrows in [Figs. 1a and 1b](#) (see [Table 1](#) for the simulation parameters). The detailed spatial structures in the true vector current fields are well observed at a grid of 1-km spatial resolution.

b. Sampling and simulating the radial velocities

A radial velocity r at a radial grid point with a bearing angle θ is presented as a sum of the projection of the two true orthogonal components (u and v) onto the bearing angle and an observational error of the radial velocity ϵ as follows:

$$r = \mathbf{u}^\dagger \mathbf{g} + \epsilon \quad (1)$$

$$= u \cos\theta + v \sin\theta + \epsilon \quad (2)$$

$$= |u + iv| \cos(\varphi - \theta) + \epsilon, \quad (3)$$

where $\mathbf{g} = [\cos\theta \sin\theta]^\dagger$ is the directional unit vector, and $\mathbf{u} = [u \ v]^\dagger$ and $\varphi = \arctan(v/u)$ denote a true vector current and its direction at the sampling location of interest, respectively († is the vector transpose or matrix transpose). Because the true vector current components are defined in a continuous horizontal space within a domain, the radial velocities at arbitrary locations are easily found via a simple mathematical conversion [Eq. (2)]. A single two-dimensional vector solution requires at least two independent radial velocity data obtained from the individual radars. For reference, a discussion of how a single radial velocity map is used to reconstruct a vector current map is presented in [appendix A](#).

1) SPACING FOR THE SPATIAL SAMPLING OF THE RADIAL VELOCITIES

The radial velocities (blue and red arrows in [Figs. 1a and 1b](#)) are sampled on polar coordinate grids that have a range spacing of 1 km ($\Delta s = 1$ km) and an azimuthal spacing of 5° ($\Delta\theta = 5^\circ$) from two radars (R1 and R2) located along the shoreline with a

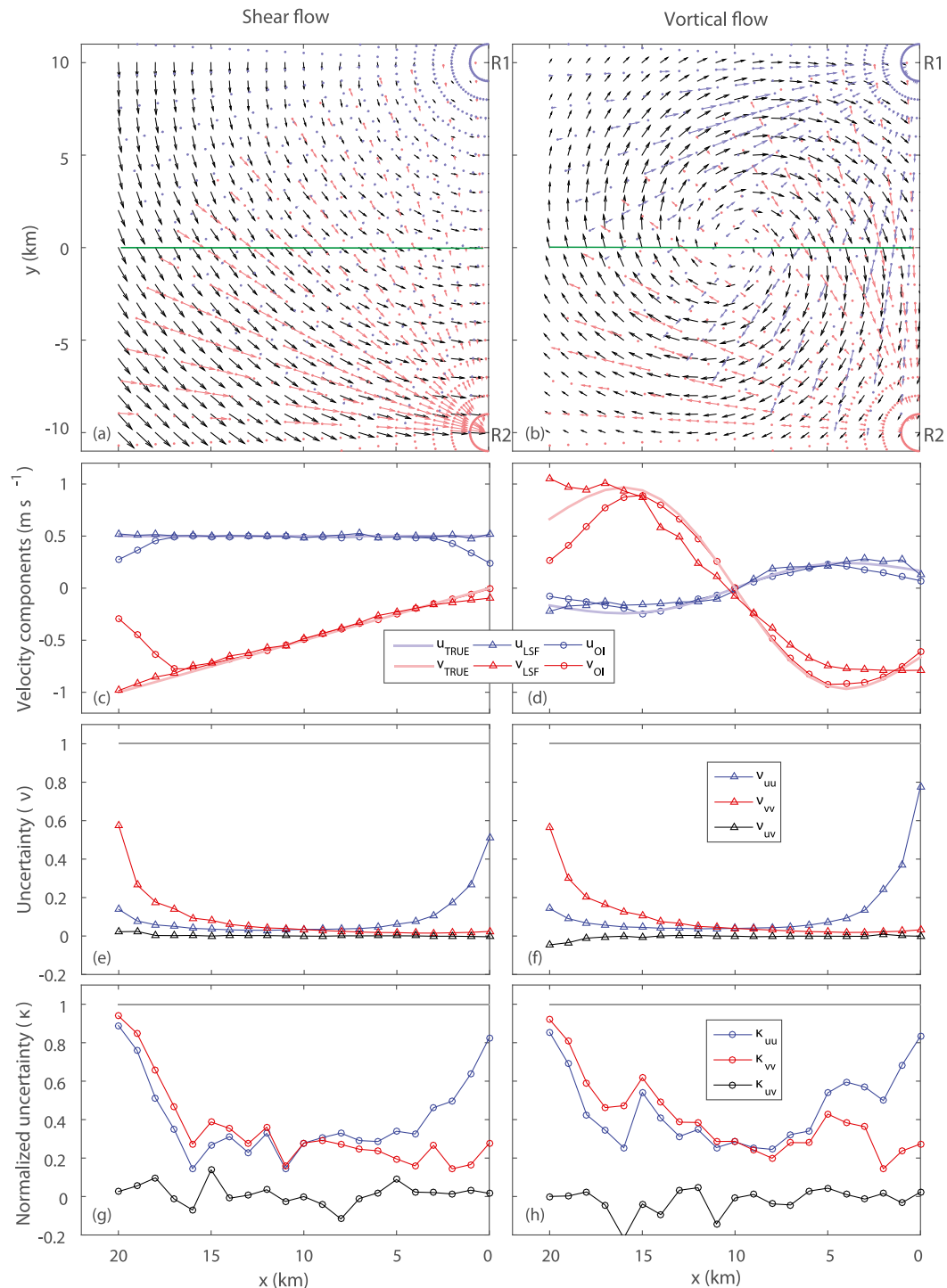


FIG. 1. (a),(b) Two examples of the simulated true vector current fields (black) having horizontal shear and vortical flow patterns on a 1-km spatial resolution grid ($\Delta x = 1$ km) and their radial velocity maps (blue and red) sampled on polar coordinate grids ($\Delta r = 1$ km, $\Delta \theta = 5^\circ$) from two radars located along the shoreline, which are separated by 20 km ($\delta = 20$ km). The radial velocity maps of the shear and vortical flow fields contain 30% ($\zeta = 0.3$) and 40% ($\zeta = 0.4$) of missing data, respectively. (c),(d) Estimated vector current components (u and v ; m s^{-1}) along a cross-shore line [green lines in (a) and (b)] using LSF and OI. An identical search radius of 4 km ($\beta_a = \beta_b = 4$ km) is applied to LSF and OI. (e),(f) GDOPs [ν for LSF; Eq. (5)]. (g),(h) Normalized uncertainties [κ for OI; Eq. (20)] (see Table 1 for the simulation parameters).

TABLE 1. Parameters in the idealized and realistic simulations in Figs. 1, 3–10, 12, 13, and B1–B3 are listed as follows: a separation distance (δ , km), range spacing (Δs , km) and azimuthal spacing ($\Delta\theta$, $^\circ$) of the radial grid, spacing of the rectangular grid (Δl , km), data quality (ζ), noise level (p), search radii (β_a and β_b , km) in LSF and OI, and an isotropic decorrelation length scale ($\lambda = \lambda_x = \lambda_y$, km) in OI. Simulations are conducted with combinations of a single parameter with discretely changing values and the rest of the parameters with a fixed value for the control simulations (boldface values for Figs. 3–10 and asterisked values for Figs. B1–B3). Note that the idealized simulations mimic the blueprint of an observational system using two 25-MHz (150-kHz bandwidth) radars, which have an effective maximum offshore range of 35 km and a range spacing of 1 km, respectively, and the true vector current fields are well resolved at a grid of 1-km spatial resolution.

Parameters	Idealized simulations			Realistic simulations	
	Fig. 1 (Fig. B1*) for a shear flow	Fig. 1 (Fig. B1*) for a vortical flow	Figs. 3–6 (Figs. B2* and B3*) and Figs. 7–10 for a vortical flow	Fig. 12	Fig. 13
δ	20	20	8, 12, 16, 20* , 24, 28, 32	—	—
Δs	1	1	0.5, 0.75, 1* , 1.25, 1.5, 1.75, 2	—	—
$\Delta\theta$	5	5	2, 3, 4, 5* , 6, 7, 8	5	5
Δl	1	1	0.5, 1* , 1.5, 2, 2.5, 3, 3.5, 4	6	6
ζ	0.3	0.4	0, 0.1, 0.2* , 0.3, 0.4, 0.5, 0.6	0, 0.2, 0.4	0.2
p	0	0	0* , 0.05, 0.1, 0.15, 0.2, 0.25	0	0.1, 0.2, 0.3
β_a	4 (1.5*)	4 (1.5*)	1, 1.5*, 2, 2.5, 3, 3.5, 4 , 4.5	5, 14	5, 14
β_b	4	4	2, 3, 4* , 5, 6, 7	14	14
λ	2	2	0.5, 1, 1.5, 2* , 2.5, 3, 3.5, 4	10	10

separation distance of 20 km ($\delta = 20$ km). The idealized simulations mimic an observational system using two 25-MHz (150-kHz bandwidth) radars that have an effective maximum offshore range of 35 km, a range spacing of 1 km, and a range of bearing angle of 130° . However, the simulated range of bearing angles (90°) and the radar maximum offshore range (20 km) may not affect the overall evaluation because we evaluate the true and estimated vector currents along a cross-shore line in the middle of the two radars under given inverse methods.

2) IMPLEMENTATION OF THE MISSING DATA AND OBSERVATIONAL ERROR OF THE RADIAL VELOCITIES

One parameter for the data quality ζ is defined as the ratio of the number of missing radial data to the number of the total radial data. Because the uncertainty varies with the data quality—that is, the conditions of the missing radial data [see section 2d(1)]—two different cases of the data quality are simulated in the horizontal shear ($\zeta = 0.3$) and vortical ($\zeta = 0.4$) flow fields, which leads to the different uncertainties in the vector current solutions.

The other parameter for the noise level p of the radial velocities is defined as the ratio of the noise variance to the variance of the true currents, which is the inverse of the signal-to-noise ratio (SNR; $p = 1/\text{SNR}$). The observational error of the radial velocities is assumed to be random noise, that is, a noise floor level of the observations regardless of any physical quantities of the true vector current field (e.g., Paduan and Graber 1997). For example, the zero observational noise of the radial velocities is applied to the simulated

flow fields ($p = 0$; Figs. 1a and 1b), which indicates the infinite SNR.

c. Spatial mapping of the radial velocities and associated uncertainty

LSF and OI are used to estimate a vector current from the multiple radial velocities. As an unbiased estimator under the assumption of an infinite SNR, LSF adopts a spatially segmented correlation function, which implies a perfect correlation between the radial velocities within a search radius β_a from a rectangular grid point of interest, and with no correlations outside of that search radius. Conversely, OI uses a spatially continuous correlation function and weights the contribution of the radial velocities as a function of distance from a rectangular grid point of interest, that is, assuming the finite SNR as a biased estimator [see Kim et al. (2008) for more details]. Although a search radius β_b is implemented in OI, it is designed to exclude the contributions of the radial velocities that have a low correlation with the radial velocity at the estimation point and to have better performance in solving inverse problems, which is different from the usage of the search radius in LSF. Because the two approaches have been investigated thoroughly elsewhere (Kim et al. 2008), we explicitly compare the uncertainties of the estimated vector currents in the two methods. Among the parameters for the vector current mapping, an identical search radius in LSF and OI is chosen as 4 km ($\beta_a = \beta_b = 4$ km) to facilitate consistent comparisons under the same conditions of the participating radial velocities within the search radius (Fig. 1; see Table 1 for the simulation parameters).

The vector current solutions are estimated on a grid of the cross-shore line with a resolution of 1 km ($\Delta l = 1$ km; a green line in Figs. 1a and 1b), which is identical to the

spacing of the true rectangular grid. The region near the baseline, which is a straight line between the two radar sites, is an area where it is not possible to estimate the vector solutions from nearly parallel radial velocities because the vector solutions normal to the baseline are weakly constrained (e.g., Lipa and Barrick 1983; Graber et al. 1997; Kim et al. 2011; Kim 2015).

1) GEOMETRIC DILUTION OF PRECISION IN LSF

A vector current ($\hat{\mathbf{u}}; 2 \times 1$ vector) estimated from radial velocities ($\mathbf{r}; L_a \times 1$ vector) using unweighted LSF is defined as

$$\hat{\mathbf{u}} = (\mathbf{G}^\dagger \mathbf{G})^{-1} \mathbf{G}^\dagger \mathbf{r} = \mathbf{H}_a \mathbf{r}, \quad (4)$$

where $\mathbf{G} = [\mathbf{g}_1 \mathbf{g}_2, \dots, \mathbf{g}_{L_a}]^\dagger$ is a concatenated matrix of the directional unit vectors of the participating radial velocities [$L_a \times 2$ matrix; Eq. (4)]. The GDOP is defined by the diagonal components of the inverse of a geometric covariance matrix ($\mathbf{G}^\dagger \mathbf{G}; 2 \times 2$ matrix) as follows:

$$\nu = (\mathbf{G}^\dagger \mathbf{G})^{-1} = \begin{bmatrix} \nu_{uu} & \nu_{uv} \\ \nu_{vu} & \nu_{vv} \end{bmatrix}, \quad (5)$$

where ν_{uu} and ν_{vv} are GDOPs in the x and y directions, respectively,

$$\nu_{uu} = \frac{1}{\det(\mathbf{G}^\dagger \mathbf{G})} \sum_{l=1}^{L_a} \sin^2 \theta_l \quad \text{and} \quad (6)$$

$$\nu_{vv} = \frac{1}{\det(\mathbf{G}^\dagger \mathbf{G})} \sum_{l=1}^{L_a} \cos^2 \theta_l, \quad (7)$$

and \det denotes the determinant of a square matrix. Thus, the total GDOP associated with L_a radial velocities is given by

$$\nu = \nu_{uu} + \nu_{vv} = \frac{L_a}{\det(\mathbf{G}^\dagger \mathbf{G})}, \quad (8)$$

which is identical to the geometrical dilution of statistical accuracy (GDOSA) normalized by the variance of current components (Barrick 2002).

The GDOP depends on 1) the number of available radial velocities (L_a) within the search radius (β_a) and 2) the difference between the bearing angles ($\Delta\theta = \theta_j - \theta_k; j$ and $k = 1, 2, \dots, L_a$) [Eqs. (6) and (7)] (e.g., O'Keefe 2005; Kim et al. 2008). For instance, the probability density functions (PDFs) of the number of HFR-derived radial velocities within the two search radii ($\beta_a = 5$ and 14 km) off Oregon for a period of two years (2007–08) show a dominance at 3 and 8, respectively (Fig. 2a). The PDFs of the corresponding GDOPs indicate smaller GDOPs for a larger number of the available radial velocities (Fig. 2b).

Similarly, the GDOPs are simulated with multiple combinations of bearing angles that have an azimuthal spacing of 1° , which is the minimum azimuthal spacing in the observations using operational HFRs. The bearing angles are uniformly generated between 0° and 360° under a given number of radial velocities for 10 000 cases. The minima L_a^{-1} and maxima s^2 of the GDOPs decrease with the number of available radial velocities [Figs. 2c and 2e; Eqs. (9) and (10)], which can be used as the upper and lower bounds of the GDOPs:

$$\frac{1}{L_a} \leq \nu_{uu} \leq s^2(L_a) \quad \text{and} \quad (9)$$

$$\frac{1}{L_a} \leq \nu_{vv} \leq s^2(L_a). \quad (10)$$

Note that the cases in which the condition number of the geometric covariance matrix ($\mathbf{G}^\dagger \mathbf{G}$) is higher than 10^{10} are excluded to ensure stable estimates in the matrix inversion (Fig. 2).

The PDFs of the GDOPs approach a lognormal distribution as the number of participating radial velocities increases (Figs. 2d and 2f). The GDOP has been used as a cutoff value for spurious and inconsistent vector estimates (e.g., Graber et al. 1997; O'Keefe 2005; Chavanne et al. 2007). The GDOP, a unit-less quantity, varies in time and space as the number of the available radial velocity data vary in time and space caused by the missing radial velocities (e.g., Chapman et al. 1997; Cook and Shay 2002; Shay et al. 2007). Thus, GDOPs should be addressed carefully when they are used as a QAQC tool in the operational system and scientific data analysis.

2) MAPPING ERRORS IN OI

A vector current ($\hat{\mathbf{u}}; 2 \times 1$ vector) is optimally interpolated from radial velocities ($\mathbf{r}; L_b \times 1$ vector) using a data–model covariance ($\text{cov}_{\text{dm}}; L_b \times 2$ matrix) and data–data covariance ($\text{cov}_{\text{dd}}; L_b \times L_b$ matrix):

$$\hat{\mathbf{u}} = \text{cov}_{\text{dm}}^\dagger \text{cov}_{\text{dd}}^{-1} \mathbf{r}, \quad (11)$$

$$= (\langle \mathbf{r} \mathbf{u}^\dagger \rangle)^\dagger (\langle \mathbf{r} \mathbf{r}^\dagger \rangle)^{-1} \mathbf{r} = \mathbf{H}_b \mathbf{r}, \quad (12)$$

where cov_{dm} is the covariance between a vector current at the grid point of interest and radial velocities, and cov_{dd} is the covariance between radial velocity data themselves.

The estimated vector currents are expressed with

$$\hat{\mathbf{u}} = (\mathbf{g}_i^\dagger \langle \mathbf{u}_i \mathbf{u}_i^\dagger \rangle)^\dagger (\mathbf{g}_j^\dagger \langle \mathbf{u}_j \mathbf{u}_j^\dagger \rangle \mathbf{g}_k + \langle \boldsymbol{\epsilon} \boldsymbol{\epsilon}^\dagger \rangle)^{-1} \mathbf{r}, \quad (13)$$

where $\hat{\mathbf{u}} = \hat{\mathbf{u}}_i = [\hat{u}_i \hat{v}_i]^\dagger$ is a vector current at the i th grid point of interest and $\mathbf{r} = [r_1 r_2, \dots, r_{L_b}]^\dagger$ is the radial velocities participating in the estimate of the vector current ($j, k = 1, 2, \dots, L_b$).

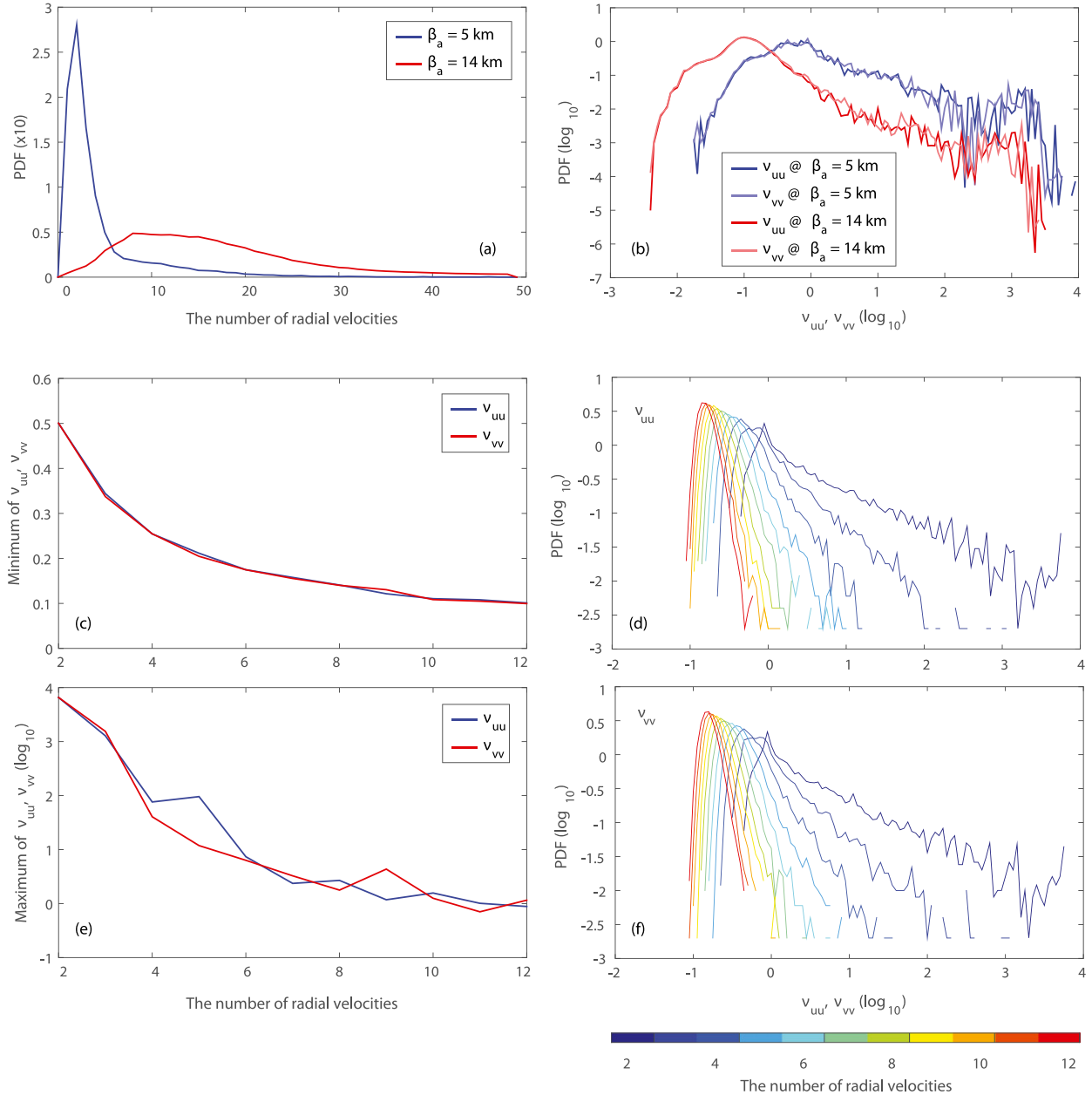


FIG. 2. (a),(b) PDFs of the number of HFR-derived radial velocities (L_a) within two search radii ($\beta_a = 5$ km and $\beta_a = 14$ km) off Oregon for a period of two years (2007–08) and the corresponding GDOPs (v_{uu} and v_{vv}) of the vector currents estimated using LSF. Shown in (c)–(f) are minima and maxima of the GDOPs (v_{uu} and v_{vv}) as a function of the number of participating radial velocities and their PDFs based on the proposed simulations. Note that the spacing of bearing angles is assumed to be 1° , and the cases where the condition number of the geometric covariance matrix ($\mathbf{G}^\dagger \mathbf{G}$) is higher than 10^{10} are excluded. (c) Minima of the GDOPs (v_{uu} and v_{vv} , linear scale). (e) Maxima of the GDOPs (v_{uu} and v_{vv} , \log_{10} scale). (d),(f) PDFs of the GDOPs (v_{uu} and v_{vv} , \log_{10} scale) as a function of the number of participating radial velocities (color); they share a color bar on the bottom.

Assuming the vector current field is locally homogeneous, the covariance of the vector current components $\langle \mathbf{u}\mathbf{u}^\dagger \rangle$ can be simplified with the standard deviations of the currents σ as a function of the location and the spatial correlation ρ as a function of the spatial lags:

$$\langle \mathbf{u}(\mathbf{x})\mathbf{u}(\mathbf{x} + \Delta\mathbf{x})^\dagger \rangle = \sigma(\mathbf{x})\sigma(\mathbf{x} + \Delta\mathbf{x})\rho(\Delta\mathbf{x}). \quad (14)$$

The error covariance $\langle \boldsymbol{\epsilon}\boldsymbol{\epsilon}^\dagger \rangle$ can be simplified as a diagonal matrix scaled by a scalar noise level (γ^2 ; a squared quantity) under an assumption of the incoherent noise of

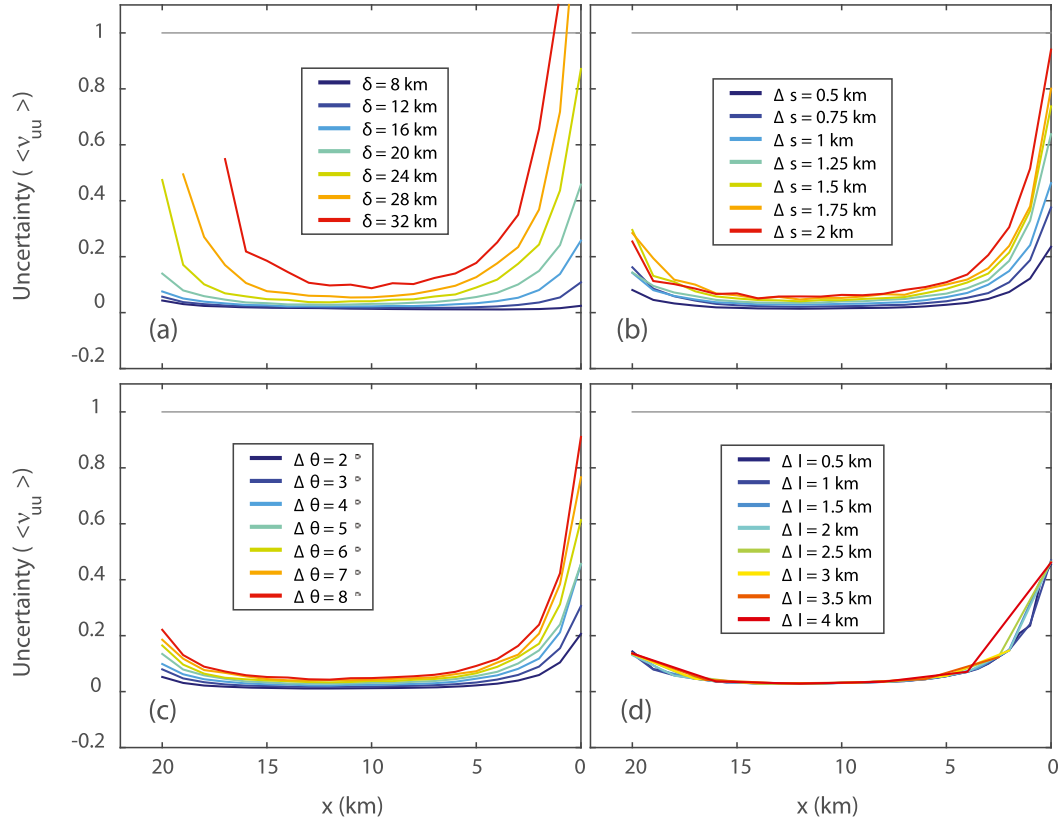


FIG. 3. Ensemble-averaged GDOPs ($\langle v_{uu} \rangle$) of the LSF-mapped u component estimated from the radial velocity maps (Fig. 1b) are evaluated with the (a) separation distance ($\delta = 8, 12, 16, 20, 24, 28,$ and 32 km), (b) range spacing ($\Delta s = 0.5, 0.75, 1, 1.25, 1.5, 1.75,$ and 2 km), (c) azimuthal spacing ($\Delta\theta = 2^\circ, 3^\circ, 4^\circ, 5^\circ, 6^\circ, 7^\circ,$ and 8°), and (d) spacing of the rectangular grid ($\Delta l = 0.5, 1, 1.5, 2, 2.5, 3, 3.5,$ and 4 km). Simulations are with combinations of a single parameter with discretely changing values and the rest of the parameters with a fixed value for the control simulations (see Table 1 for the simulation parameters).

the radial velocities at individual radial grid points. The noise level varies in time and space depending on the sea state, the external noise from the ionospheric effects or other radio-frequency transmitters nearby, the repair state of the electronics, and the aging of the receiving antenna. However, a constant value representing the noise level over the given period (e.g., two years) is applied in this paper. For instance, a standard deviation of the sum of the nearby radial pairs obtained from multiple radars [see Kim et al. (2008) and Kim (2015) for more details]—that is, the sum of the sampling error and the measurement error of the observed radial velocities in the area of interest—is used as γ .

Thus, the estimated vector currents $\hat{\mathbf{u}}$ are given by

$$\hat{\mathbf{u}} = \left[\mathbf{g}_i^\dagger \sigma_i \sigma_j \rho(\Delta x_{ij}, \Delta y_{ij}) \right]^\dagger \left[\mathbf{g}_j^\dagger \sigma_j \sigma_k \rho(\Delta x_{jk}, \Delta y_{jk}) \mathbf{g}_k + \delta_{jk} \gamma^2 \right]^{-1} \mathbf{r}, \quad \chi = \frac{\gamma^2}{\sigma^2} (\text{cov}_{\text{mm}} - \text{cov}_{\text{dm}}^\dagger \text{cov}_{\text{dd}}^{-1} \text{cov}_{\text{dm}}) = \begin{bmatrix} \chi_{uu} & \chi_{uv} \\ \chi_{vu} & \chi_{vv} \end{bmatrix}, \quad (15)$$

where δ_{jk} denotes the Kronecker delta, and the variance of currents at individual locations of i and j can be approximated with the variance of currents, that is, $\sigma_i \sigma_j = \sigma_j \sigma_k \approx \sigma^2$.

An example of the exponential correlation function $[\rho(\Delta x, \Delta y)]$, which is frequently used for mapping sub-mesoscale surface current fields (e.g., Kim et al. 2008, 2011), is derived as follows:

$$\rho(\Delta x, \Delta y) = \exp\left(-\sqrt{\frac{\Delta x^2}{\lambda_x^2} + \frac{\Delta y^2}{\lambda_y^2}}\right), \quad (16)$$

where λ_x and λ_y denote the decorrelation length scales in the x and y directions, respectively.

The uncertainty χ of the optimally interpolated vector currents, which corresponds to Eq. (5) in LSF, is defined as

where

$$0 \leq \chi_{uu} \leq \gamma^2 \quad \text{and} \quad (18)$$

$$0 \leq \chi_{vv} \leq \gamma^2. \quad (19)$$

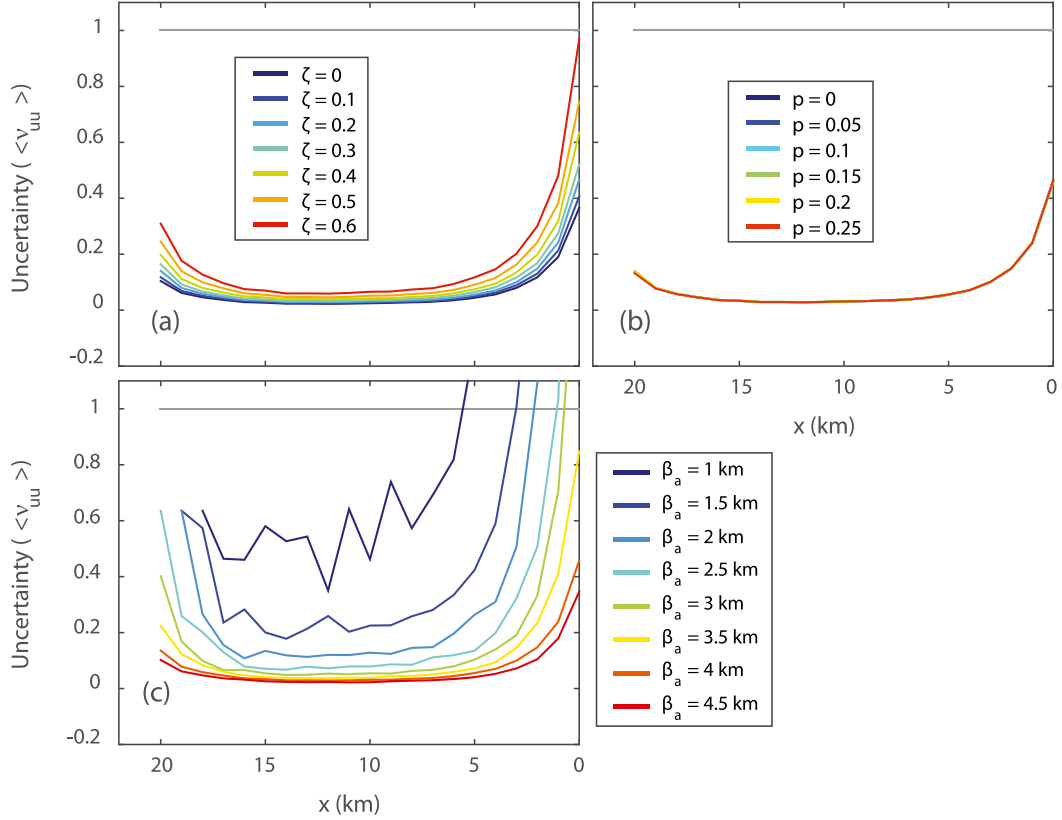


FIG. 4. Ensemble-averaged GDOPs ($\langle v_{uu} \rangle$) of the LSF-mapped u component estimated from the radial velocity maps (Fig. 1b) are evaluated with the (a) data quality ($\zeta = 0, 0.1, 0.2, 0.3, 0.4, 0.5,$ and 0.6), (b) noise level ($p = 0, 0.05, 0.1, 0.15, 0.2,$ and 0.25), and (c) search radius ($\beta_a = 1, 1.5, 2, 2.5, 3, 3.5, 4,$ and 4.5 km). Simulations are with combinations of a single parameter with discretely changing values and the rest of the parameters with a fixed value for the control simulations (see Table 1 for the simulation parameters).

Note that χ has the units of velocity squared. Additionally, the normalized uncertainty κ ($0 \leq \kappa \leq 1$) is given by

$$\kappa = \frac{\chi}{\gamma^2} = \begin{bmatrix} \kappa_{uu} & \kappa_{uv} \\ \kappa_{vu} & \kappa_{vv} \end{bmatrix}, \quad (20)$$

which is used as a criterion for QAQC of the estimated vector currents.

d. Evaluation

1) OVERVIEW

We consider the uncertainty [ϵ_e in Eq. (21)] and misfit [\mathbf{u}_e in Eq. (23)] as metrics in the evaluation of the reconstruction performance and evaluate them in terms of 1) a separation distance (δ) between the two radars located along the shoreline (y direction), 2) a range spacing (Δs) and 3) an azimuthal spacing ($\Delta\theta$) of the identical radial grids of the two radars, 4) a constant spacing of the rectangular grid (Δl), 5) an indicator of the data quality (ζ), 6) an observational noise parameter (p) of the radial velocities,

7) the search radii (β_a and β_b) in LSF and OI, and 8) an isotropic decorrelation length scale ($\lambda = \lambda_x = \lambda_y$) in OI (see Table 1 for the simulation parameters):

$$\epsilon_e = \epsilon_e(\delta, \Delta s, \Delta\theta, \Delta l, \zeta, p, \beta_a, \beta_b, \lambda) \quad \text{and} \quad (21)$$

$$\mathbf{u}_e = \mathbf{u}_e(\delta, \Delta s, \Delta\theta, \Delta l, \zeta, p, \beta_a, \beta_b, \lambda) \quad (22)$$

$$= \hat{\mathbf{u}} - \mathbf{u}. \quad (23)$$

The uncertainty of the vector current is a mathematical definition of the degrees of insufficiency to resolve the true vector current, which is determined by the participating radial velocities in the estimate of the vector current components. In other words, the uncertainty depends on 1) the difference of the bearing angles of the radial velocities, 2) the spatial configuration at the radial grid points (the constellation of the radar system), and 3) the observational noise of the radial velocities. If the radial velocities participating in estimating the vector currents at a fixed location are identical, the uncertainty should be the same. Thus, the

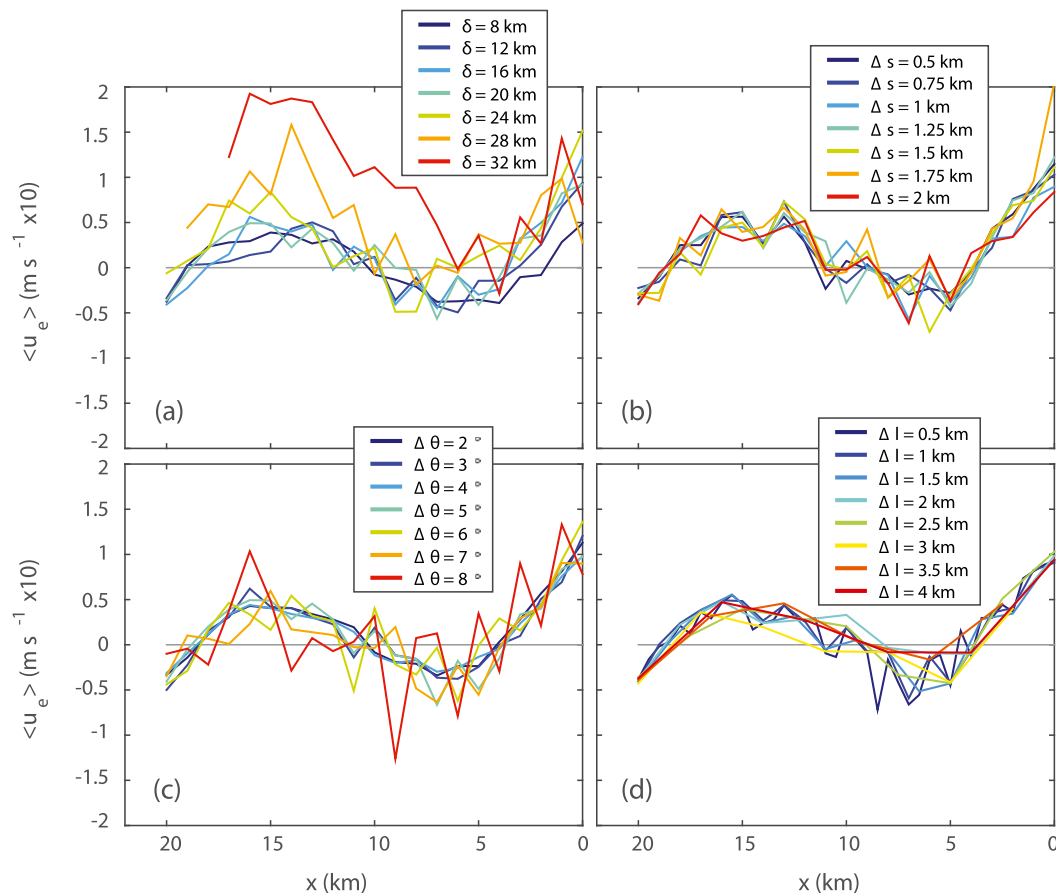


FIG. 5. Ensemble-averaged misfits ($\langle u_e \rangle \times 10; \text{m s}^{-1}$) of the LSF-mapped u component estimated from the radial velocity maps (Fig. 1b) are evaluated with the (a) separation distance ($\delta = 8, 12, 16, 20, 24, 28,$ and 32 km), (b) range spacing ($\Delta s = 0.5, 0.75, 1, 1.25, 1.5, 1.75,$ and 2 km), (c) azimuthal spacing ($\Delta \theta = 2^\circ, 3^\circ, 4^\circ, 5^\circ, 6^\circ, 7^\circ,$ and 8°), and (d) spacing of the rectangular grid ($\Delta l = 0.5, 1, 1.5, 2, 2.5, 3, 3.5,$ and 4 km). Simulations are conducted with combinations of a single parameter with discretely changing values and the rest of the parameters with a fixed value for the control simulations (see Table 1 for the simulation parameters).

uncertainty varies with the conditions of the missing radial velocities, which can be distributed in a non-systematic or random way in time and space. However, the misfit is defined as the difference between the true and estimated values in this paper. Thus, the uncertainty and misfit can be consistent or inconsistent. For instance, a greater number of radial velocities and a favorable combination of the bearing angles and geographical constellation for resolving the vector current correspond to a smaller uncertainty, although they may not guarantee the magnitude of the misfit because the estimated vector currents can be close to or different from the true vector currents.

The uncertainty ($\epsilon_e; \nu$ or κ) of the vector current includes the mapping error and systematic error. The uncertainty ν of the LSF-mapped vector currents is represented with the GDOP without the mapping error resulting from no spatial smoothing under the infinite SNR, and the

uncertainty κ of the OI-mapped vector currents is incorporated with both mapping error and systematic error.

2) EXAMPLES OF THE ESTIMATED VECTOR CURRENTS, (NORMALIZED) UNCERTAINTY, AND MISFIT

Examples of the comparison between the true and estimated vector current components and their (normalized) uncertainty along a cross-shore line under the simulation parameters in Table 1 using LSF and OI are shown in Figs. 1c–h.

Near the baseline ($x \leq 5$ km), both LSF- and OI-mapped u components, normal to the baseline, have a high uncertainty and misfit. Conversely, the OI-mapped v components, parallel to the baseline, have less misfit than the LSF-mapped v components, although the (normalized) uncertainty from both approaches is relatively small.

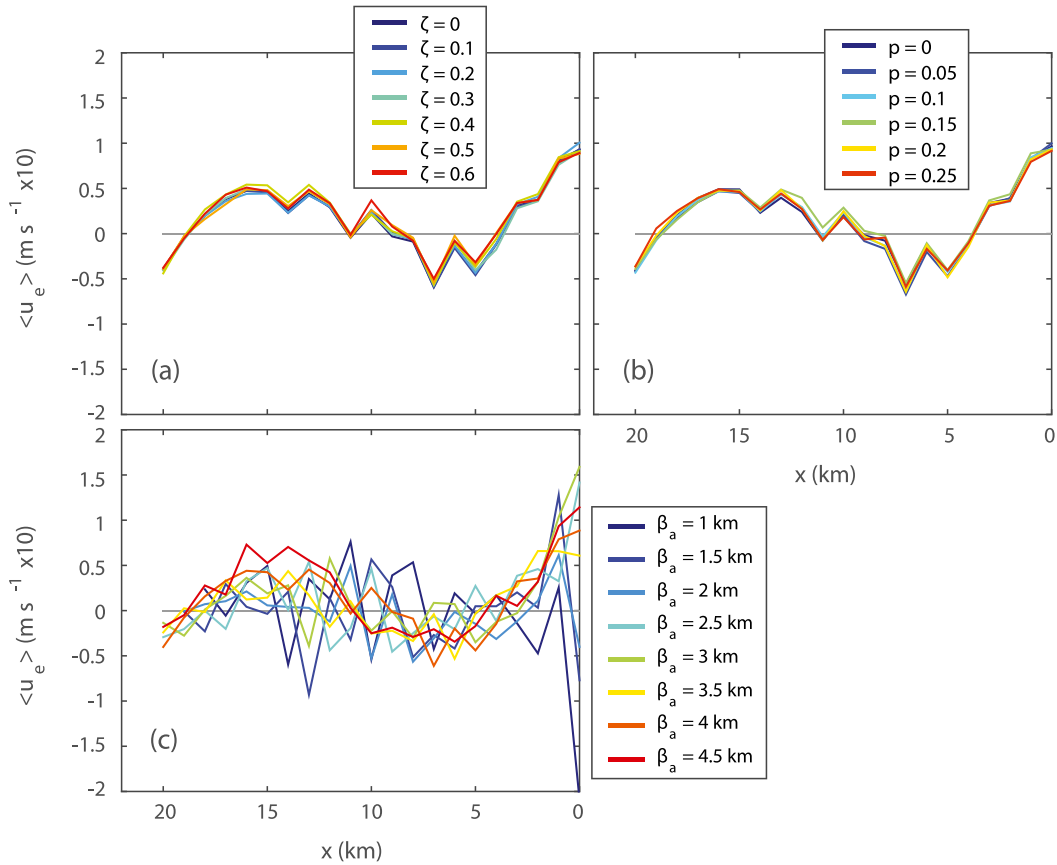


FIG. 6. Ensemble-averaged misfits ($\langle u_e \rangle \times 10$; $m s^{-1}$) of the LSF-mapped u component estimated from the radial velocity maps (Fig. 1b) are evaluated with the (a) data quality ($\zeta = 0, 0.1, 0.2, 0.3, 0.4, 0.5$, and 0.6), (b) noise level ($p = 0, 0.05, 0.1, 0.15, 0.2$, and 0.25), and (c) search radius ($\beta_a = 1, 1.5, 2, 2.5, 3, 3.5, 4$, and 4.5 km). Simulations are conducted with combinations of a single parameter with discretely changing values and the rest of the parameters with a fixed value for the control simulations (see Table 1 for the simulation parameters).

Near the edge of the domain ($x > 15$ km), the OI-mapped vector components tend to converge to zero, and the LSF-mapped vector components are close to the true values or have spurious values because insufficient radial velocity data are available in that region (Figs. 1c and 1d). The uncertainty of the v components is higher than that of the u components in both LSF and OI (Figs. 1g and 1h).

In the middle of the domain ($5 < x \leq 15$ km), the uncertainty of the estimated vector components is relatively small because the density of the overlapped radial velocities from the two independent radars is higher than that in the other sampling regions. However, the LSF-mapped vector components have more bias when compared with the true values (particularly the v component) than the OI-mapped ones (Fig. 1d). Although the significant bias of the magnitude and direction of the currents in the center of the vortex can be expected, the uncertainty is dominantly governed by the size of the overlapped area of the two radial velocity maps and is less sensitive to the flow pattern.

Because the GDOPs and uncertainty depend on the number of the available radial velocities within the search radius and the difference of their bearing angles, the differences between Figs. 1e and 1f (Figs. 1g and 1h) result from the fraction of missing data ($\zeta = 0.3$ in Figs. 1e and 1g; $\zeta = 0.4$ in Figs. 1f and 1h).

3) COMPARISON OF THE VECTOR CURRENTS ESTIMATED USING LSF AND OI UNDER VARYING PARAMETERS

For the simplicity and efficiency of evaluation, the ensemble-averaged (normalized) uncertainty ($\langle v_{uu} \rangle$ or $\langle \kappa_{uu} \rangle$) and misfit ($\langle u_e \rangle$) of the LSF- and OI-mapped u components obtained from the radial velocity maps in Fig. 1b are examined with all seven (eight) parameters in Eqs. (21) and (22), which are used in the estimates using LSF (OI) in the idealized simulations (Table 1; Figs. 3–10). Each ensemble member is realized independently 100 times, which provides stable simulation results to minimize the biased influence of the data quality because of the

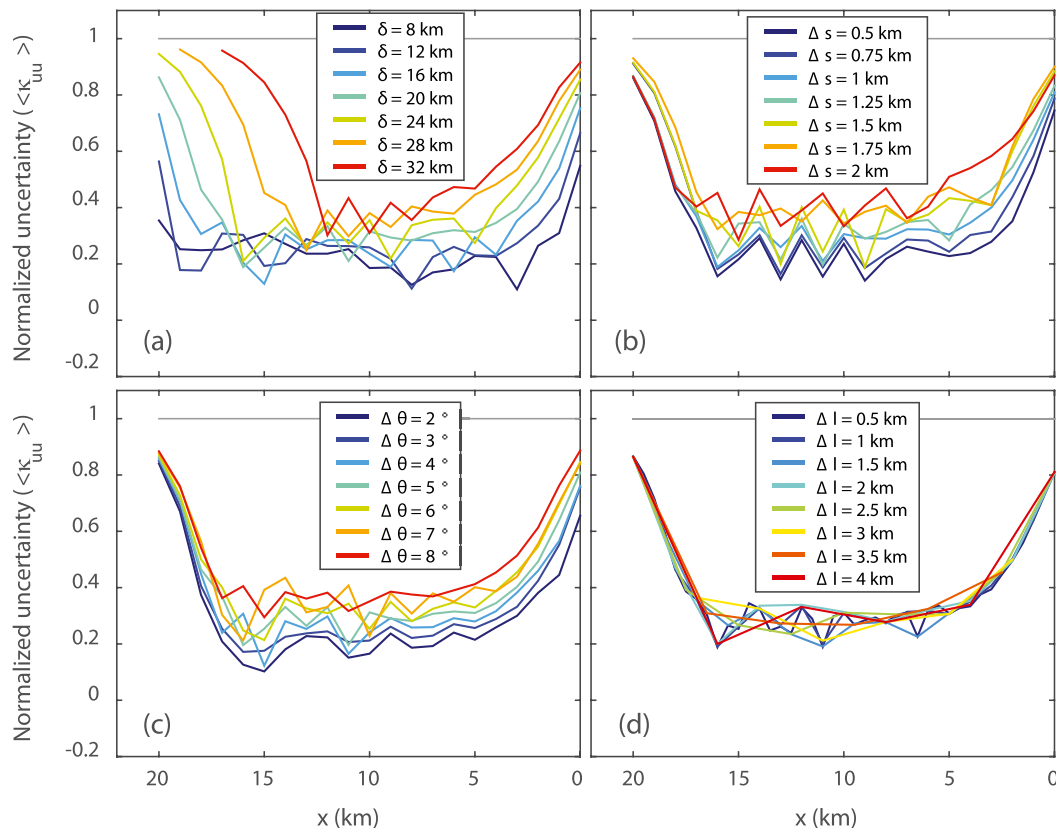


FIG. 7. Ensemble-averaged normalized uncertainties ($\langle \kappa_{uu} \rangle$) of the OI-mapped u component estimated from the radial velocity maps (Fig. 1b) are evaluated with the (a) separation distance ($\delta = 8, 12, 16, 20, 24, 28,$ and 32 km), (b) range spacing ($\Delta s = 0.5, 0.75, 1, 1.25, 1.5, 1.75,$ and 2 km), (c) azimuthal spacing ($\Delta \theta = 2^\circ, 3^\circ, 4^\circ, 5^\circ, 6^\circ, 7^\circ,$ and 8°), and (d) spacing of the rectangular grid ($\Delta l = 0.5, 1, 1.5, 2, 2.5, 3, 3.5,$ and 4 km). Simulations are conducted with combinations of a single parameter with discretely changing values and the rest of the parameters with a fixed value for the control simulations (see Table 1 for the simulation parameters).

randomly distributed missing data. The individual simulations are conducted with combinations of a single parameter with discretely changing values and the rest of the parameters with a fixed value for the control simulations (boldface or asterisked values in Table 1).

In mapping of the u component using LSF (Figs. 3–6), the ensemble-averaged uncertainty increases significantly onshore and gradually offshore with an increase of the given parameters (Figs. 3 and 4). The ensemble-averaged misfit has an organized tendency to overestimate ($10 < x \leq 20$ km and $x \leq 5$ km) and underestimate ($5 < x \leq 10$ km) as the given parameters increase (Figs. 5 and 6). The shorter separation distance between the radars yields less uncertainty and misfit because of better geometry in the constellation of the radars to resolve the currents (Figs. 3a and 5a). The smaller range and azimuthal spacings lead to less uncertainty as more radial velocities within the given search radius participate in the estimate (Figs. 3b and 3c). Similarly, the better data quality yields less uncertainty (Fig. 4a). However, the misfit is barely

influenced by the spacing of the range, azimuth, rectangular grid, data quality, and noise level because the radial velocities within the given search radius are sufficient to resolve the currents (Figs. 5b–d, 6a, and 6b). The reduced search radius yields higher uncertainty and misfit, which can be considered as the most sensitive factor affecting the performance in the estimate of the vector currents (Figs. 4c and 6c).

In mapping of the u component using OI (Figs. 7–10), the quality of the estimated vector currents degrades with longer separation distance between the radars because the shorter separation distances yield the higher density of the overlapped radial velocities and the better geometry by which to resolve the vector currents (Figs. 7a and 9a). However, a separation distance of less than 6 km hinders resolving the flow fields because of the inefficient constellation of the radar bearing angles. When the range and azimuthal spacings increase, the ensemble-averaged normalized uncertainty and misfit increase because the radial velocity maps may not

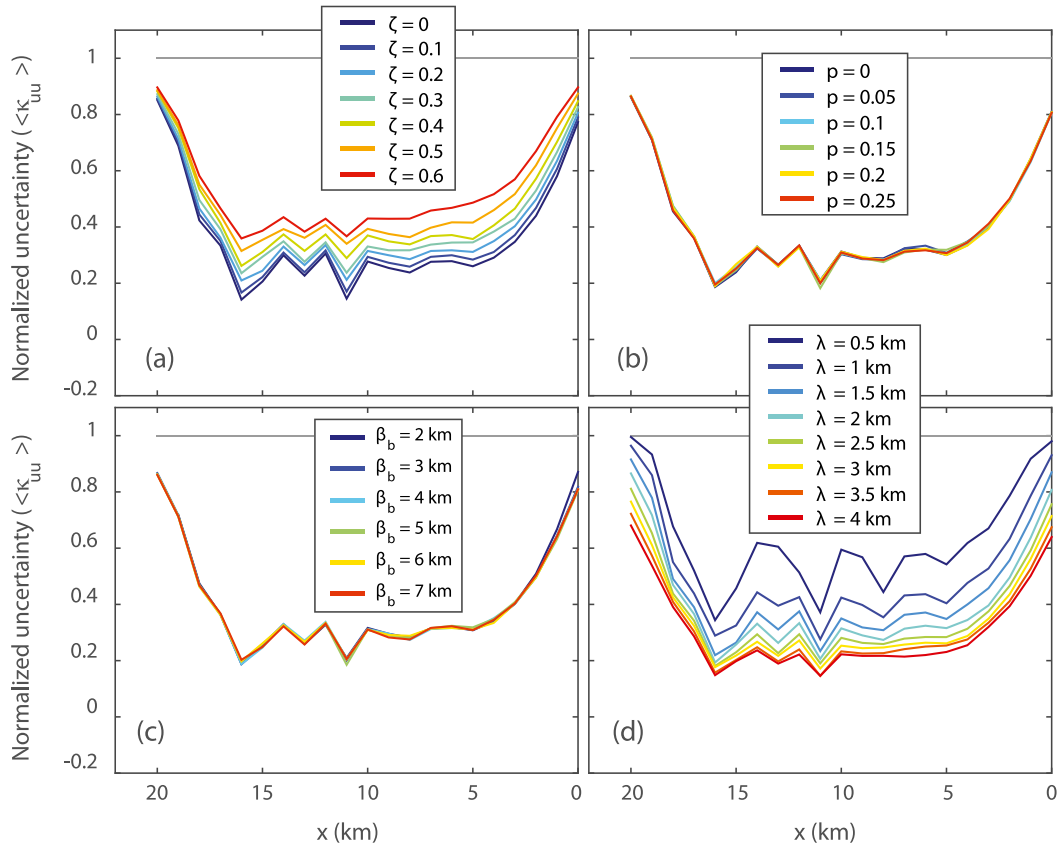


FIG. 8. Ensemble-averaged normalized uncertainties ($\langle \kappa_{uu} \rangle$) of the OI-mapped u component estimated from the radial velocity maps (Fig. 1b) are evaluated with the (a) data quality ($\zeta = 0, 0.1, 0.2, 0.3, 0.4, 0.5$, and 0.6), (b) noise level ($p = 0, 0.05, 0.1, 0.15, 0.2$, and 0.25), (c) search radius ($\beta_b = 2, 3, 4, 5, 6$, and 7 km), and (d) an isotropic decorrelation length scale ($\lambda = \lambda_x = \lambda_y = 0.5, 1, 1.5, 2, 2.5, 3, 3.5$, and 4 km). Simulations are conducted with combinations of a single parameter with discretely changing values and the rest of the parameters with a fixed value for the control simulations (see Table 1 for the simulation parameters).

resolve the given flow fields at these sampling scales (Figs. 7b, 7c, 9b, and 9c). The spacing of the rectangular grid does not significantly affect the uncertainty and misfit (Figs. 7d and 9d). The uncertainty and misfit are highly dependent on the quality of the radial velocity map, that is, the greater fraction of the missing radial velocity data leads to the higher uncertainty and misfit (Figs. 8a and 10a). Moreover, the uncertainty and misfit are not improved with decorrelation length scales longer than 3 km because the dominant features of the given flow field are well resolved at that scale and the spatial smoothing in the estimated flow fields can be minimal (Figs. 8b and 10b). Although the uncertainty is nearly constant regardless of the search radius (β_b), the misfit decreases with the search radius (Figs. 8c and 10c) because more radial velocities are participating to resolve the flow fields and those radial velocities do not contribute that much to effectively estimating the true value. However, because the search radius in OI is designed to reduce the computational burden in the

matrix inversion, its influence may not be considered as a primary factor. When longer decorrelation length scales are applied, the estimated u component has less uncertainty and misfit (Figs. 8d and 10d).

4) SUMMARY

To make a sizable comparison of the (normalized) uncertainty and misfit of the LSF- and OI-mapped vector currents, we chose the identical search radii ($\beta_a = \beta_b = 4$ km), which are 4 times as long as the rectangular grid spacing ($\Delta l = 1$ km). In OI, this search radius barely affects the estimates because the correlation at the search radius is reduced effectively. Conversely, the LSF-mapped vector currents under this search radius may yield a spatially smooth field and less uncertainty because a greater number of radial velocities participate in the vector current estimates. Thus, a reduced search radius in LSF may be required to avoid oversampling in the estimate of vector currents. The examples of the estimated vector current

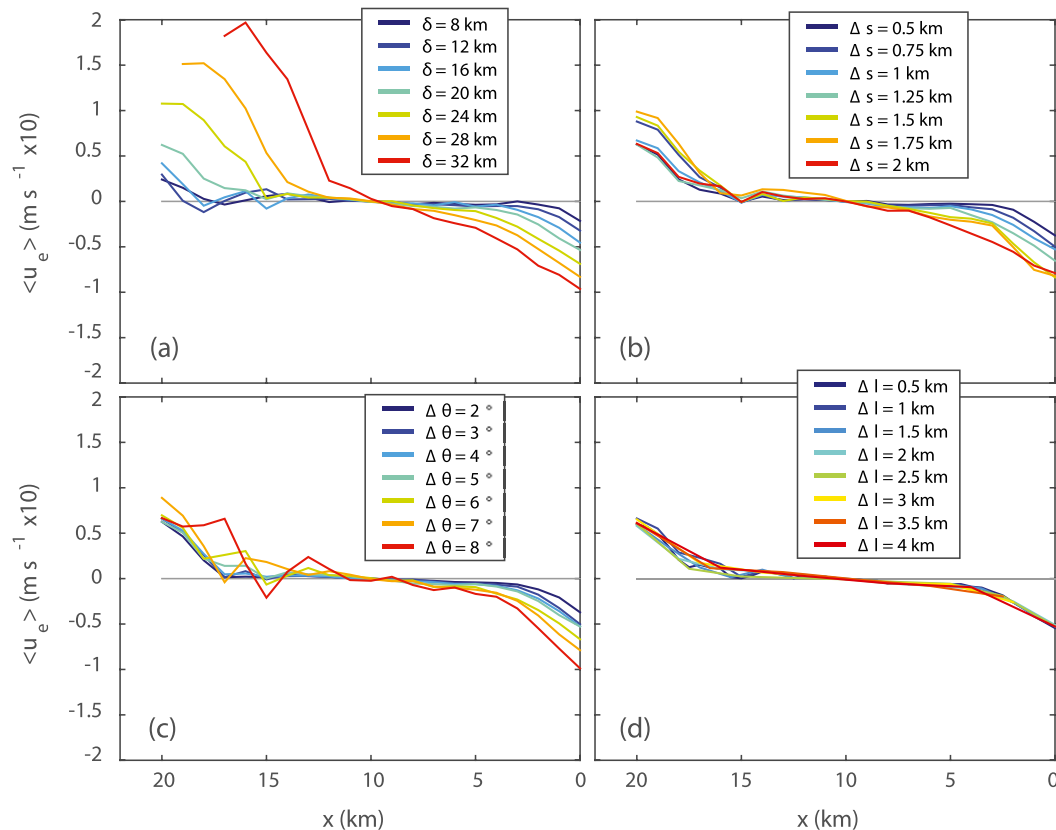


FIG. 9. Ensemble-averaged misfits ($\langle u_e \rangle \times 10$; m s^{-1}) of the OI-mapped u component estimated from the radial velocity maps (Fig. 1b) are evaluated with the (a) separation distance ($\delta = 8, 12, 16, 20, 24, 28,$ and 32 km), (b) range spacing ($\Delta s = 0.5, 0.75, 1, 1.25, 1.5, 1.75,$ and 2 km), (c) azimuthal spacing ($\Delta \theta = 2^\circ, 3^\circ, 4^\circ, 5^\circ, 6^\circ, 7^\circ,$ and 8°), and (d) spacing of the rectangular grid ($\Delta l = 0.5, 1, 1.5, 2, 2.5, 3, 3.5,$ and 4 km). Simulations are conducted with combinations of a single parameter with discretely changing values and the rest of the parameters with a fixed value for the control simulations (see Table 1 for the simulation parameters).

components and uncertainty under the reduced search radius ($\beta_a = 1.5$ km) are discussed in appendix B. In addition, the misfit of the LSF-mapped u component is more biased in space than the misfit of the OI-mapped u component is (Figs. 3–10). In other words, the smoothly estimated vector currents can be different from the true vector currents. Thus, the uncertainty decreases and the misfit becomes significantly large with an increase in the search radius. The uncertainty and misfit can be consistent or inconsistent depending on the given information to extract the vector currents and the spatial scales to fit under the chosen inverse methods.

3. Realistic numerical model

a. True vector currents

A realistic numerical simulation, using a Regional Ocean Modeling System (ROMS) off the coast of Oregon and Washington, provides maps of the surface currents (at the surface layer) with 1-h temporal and 2-km spatial resolutions

for approximately one year (August 2008–August 2009) [see Kim et al. (2014) for more details]. The simulation included the freshwater discharge from the Columbia River. Although the model outputs and time intervals for the internal calculation have much finer temporal and spatial resolutions, they are sampled at these resolutions (hourly in time and 1-km scale in space) for the present work. With the same approach as conducted in the idealized simulations (section 2a), the numerical model outputs are used as the substitutes for the true vector currents [see Eq. (3)].

Because the baselines are nearly aligned and embedded in the concave coast of Oregon, the baseline inconsistency and bad geometry in the radar constellation appear near the coast and the edge of the domain, where the nearly parallel radial velocities are found.

b. Sampling and simulating radial velocities

In the realistic simulations, the first four parameters [$\delta, \Delta s, \Delta \theta,$ and Δl in Eqs. (21) and (22); Table 1] are predetermined

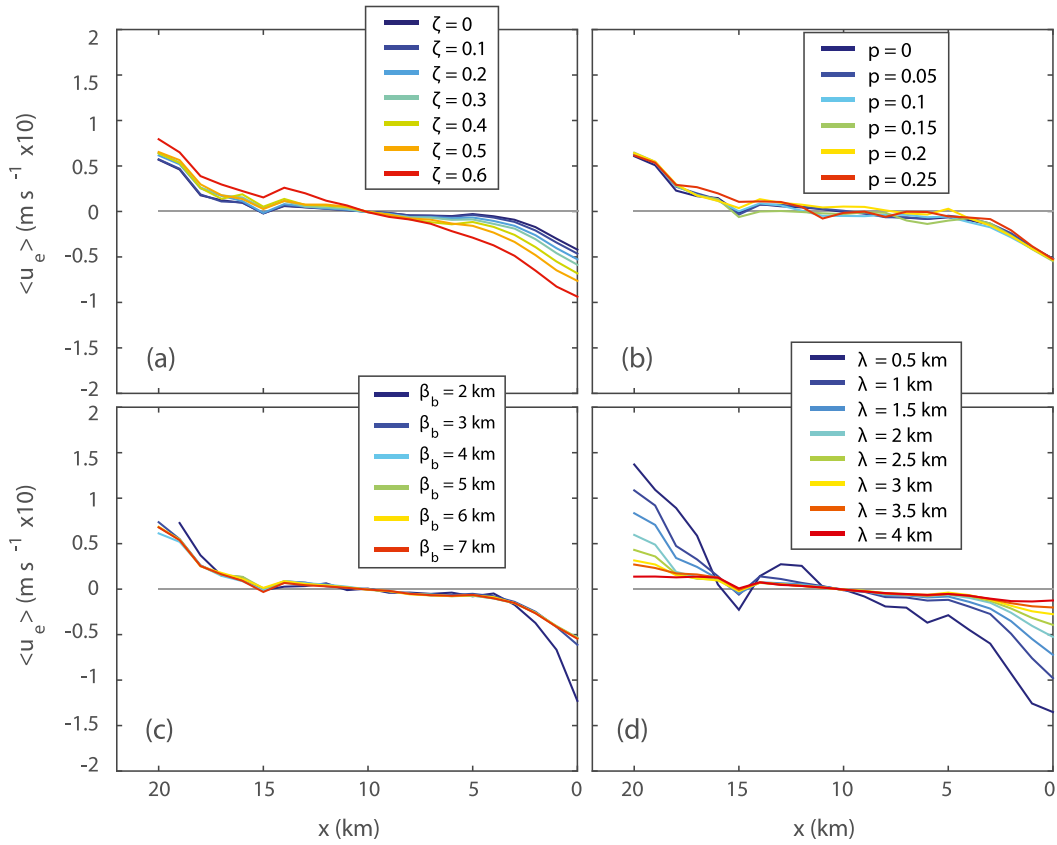


FIG. 10. Ensemble-averaged misfits ($\langle u_e \rangle \times 10$; $m s^{-1}$) of the OI-mapped u component estimated from the radial velocity maps (Fig. 1b) are evaluated with the (a) data quality ($\zeta = 0, 0.1, 0.2, 0.3, 0.4, 0.5,$ and 0.6), (b) noise level ($p = 0, 0.05, 0.1, 0.15, 0.2,$ and 0.25), (c) search radius ($\beta_b = 2, 3, 4, 5, 6,$ and 7 km), and (d) an isotropic decorrelation length scale ($\lambda = \lambda_x = \lambda_y = 0.5, 1, 1.5, 2, 2.5, 3, 3.5,$ and 4 km). Simulations are conducted with combinations of a single parameter with discretely changing values and the rest of the parameters with a fixed value for the control simulations (see Table 1 for the simulation parameters).

because of limitations on the allocation of the operating frequencies and bandwidths, and the choice of the HFR installation related to the geographical permission. Thus, the remaining parameters are simulated for the standard

deviation of the misfit (see section 3d). In this subsection we report the spatial and temporal spacings in the operational HFR-derived radial velocity maps and describe the procedures to implement the missing data and observational

TABLE 2. Detailed specifications of HFRs participating in the hindcast analysis are listed with the station name (regional name), operating frequency (f_o ; MHz), and transmitted bandwidth (f_b ; kHz) of HFRs; and the range spacing (Δs ; km), azimuthal spacing ($\Delta\theta$; $^\circ$), temporal spacing (Δt ; h), and averaging time window (Δt_w ; h) of radial velocities; and the type of the radar beam pattern [measured (M) and ideal (I)].

Station name (regional name)	f_o	f_b	Δs	$\Delta\theta$	Δt	Δt_w	Radar beam patterns
LOO1 (Loomis Lake)	4.412	25.73	5.851	5	1.00	3.00	M
STV2 (Fort Stevens)	12.157	75.07	1.998	5	1.00	1.25	M
SEA1 (Seaside)	12.247	75.07	1.998	5	1.00	1.25	M
MAN1 (Manhattan Beach)	4.785	25.73	5.829	5	1.00	3.00	M
YHL1 (Yaquina Head)	4.785	25.73	5.825	5	1.00	3.00	M
YHS2 (Yaquina Head South)	12.157	75.07	1.998	5	1.00	1.25	M
WLD2 (Waldport)	12.233	75.07	1.998	5	1.00	1.25	I
WSH1 (Washburne)	12.147	75.07	1.998	5	1.00	1.25	M
WIN1 (Winchester Bay)	4.785	25.73	5.829	5	1.00	3.00	M
CBL1 (Cape Blanco)	4.785	25.73	5.829	5	1.00	3.00	I
PSG1 (Point St. George)	4.785	25.73	5.829	5	1.00	3.00	I

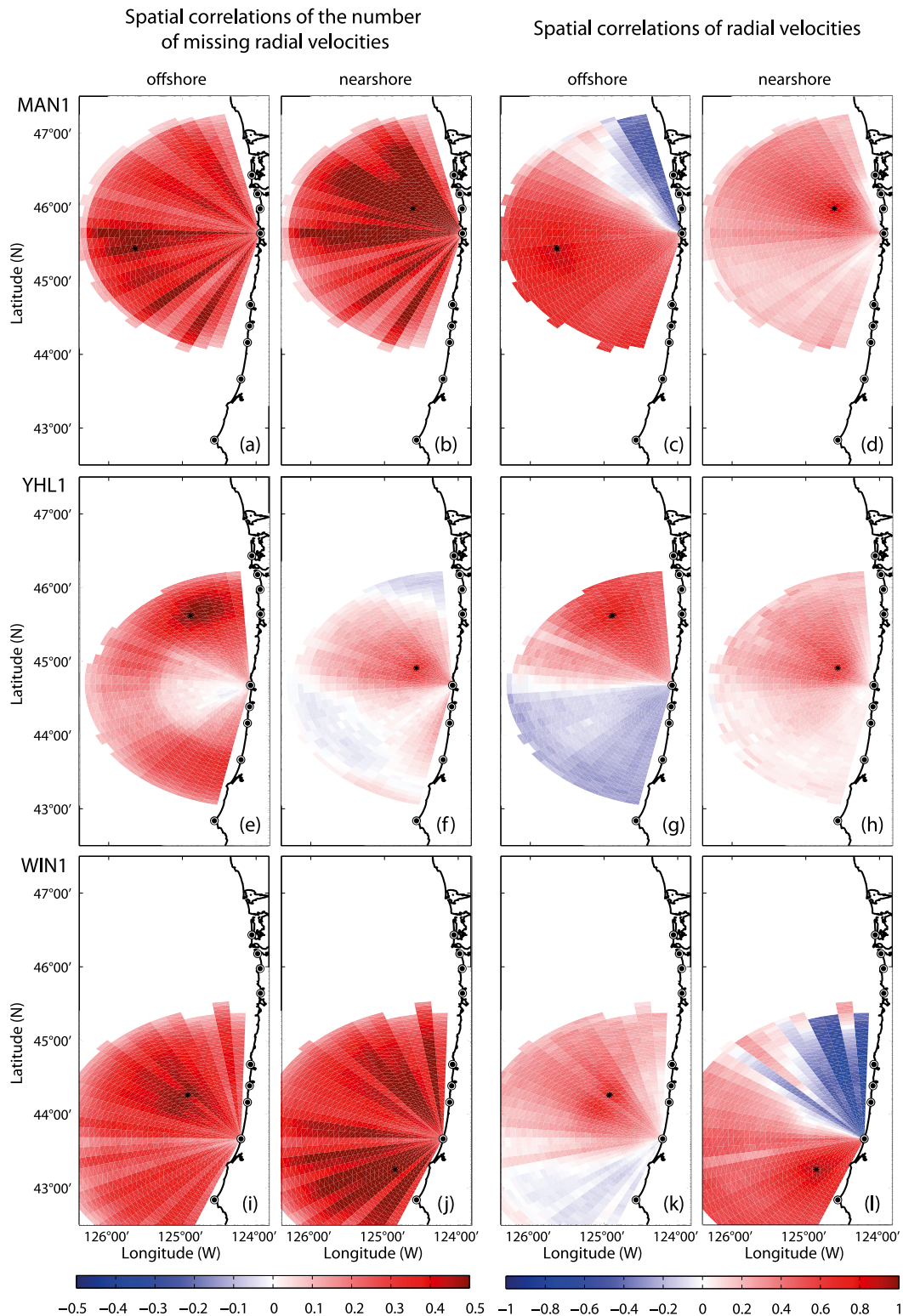


FIG. 11. (a),(b),(e),(f),(i),(j) Spatial correlations of the number of missing radial velocities. (c),(d),(g),(h),(k),(l) Spatial correlations of radial velocities. Two reference locations (black star; offshore and nearshore regions) at each radar site are chosen to present the spatial structure of correlations. Correlations are shown for (top) MAN1, (middle) YHL1, and (bottom) WIN1. All estimates are based on radial velocities at three radar sites off the Oregon coast for a period of two years (2007–08).

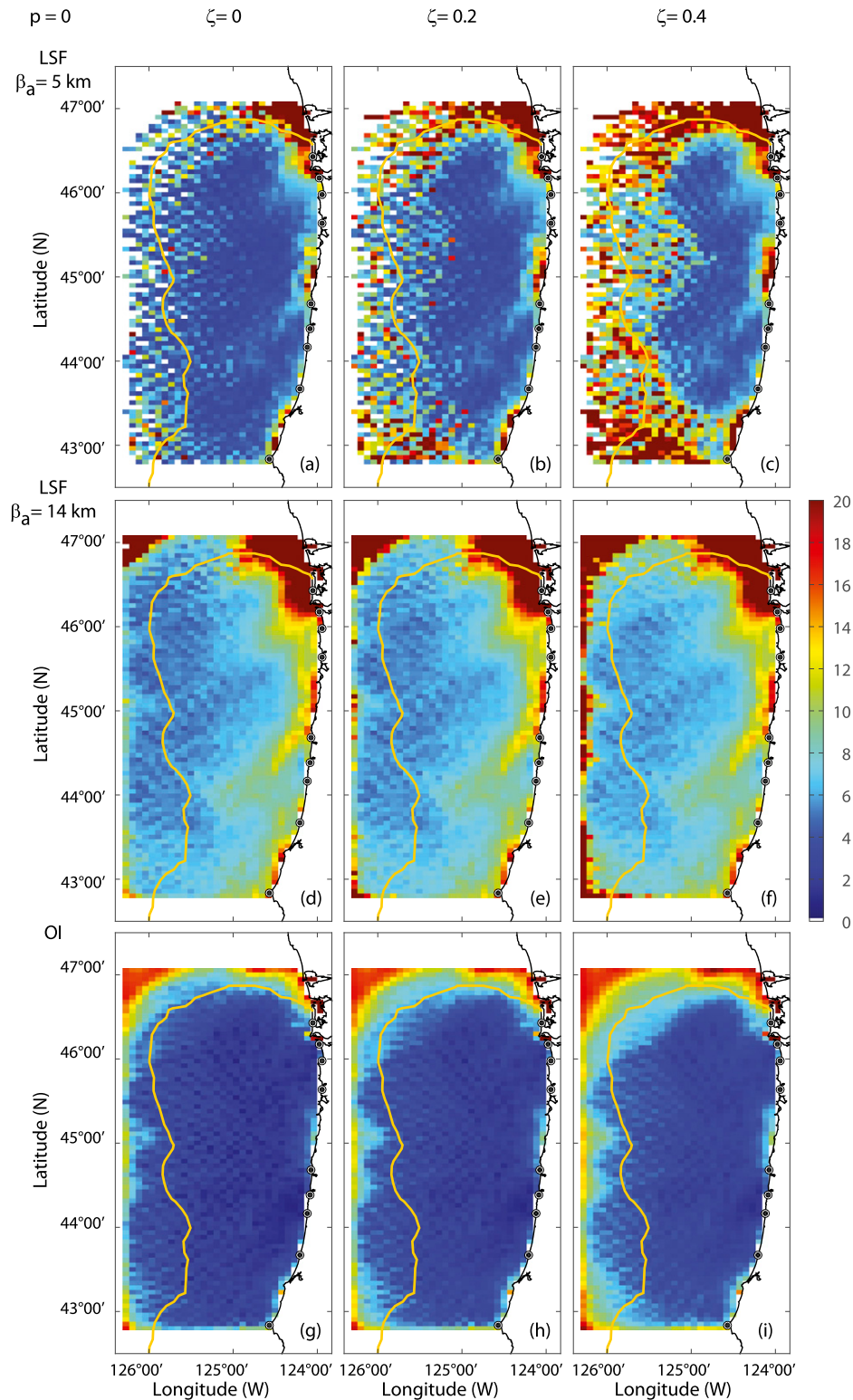


FIG. 12. Standard deviation (ξ ; cm s^{-1}) of the misfit between the estimated (LSF- and OI-mapped) and true vector currents as a function of the data quality (ζ) without observational noise ($p = 0$). All vector current maps are estimated on a grid having a 6-km spatial spacing ($\Delta l = 6$ km). (top) LSF-mapped vector current fields ($\beta_a = 5$ km). (middle) LSF-mapped vector current fields ($\beta_a = 14$ km). (bottom) OI-mapped vector current fields. (a),(d),(g) $\zeta = 0$. (b),(e),(h) $\zeta = 0.2$. (c),(f),(i) $\zeta = 0.4$ (see Table 1 for the simulation parameters). A yellow contour in the individual figures indicates the effective spatial coverage of HFRs off the Oregon coast for a period of two years (2007–08).

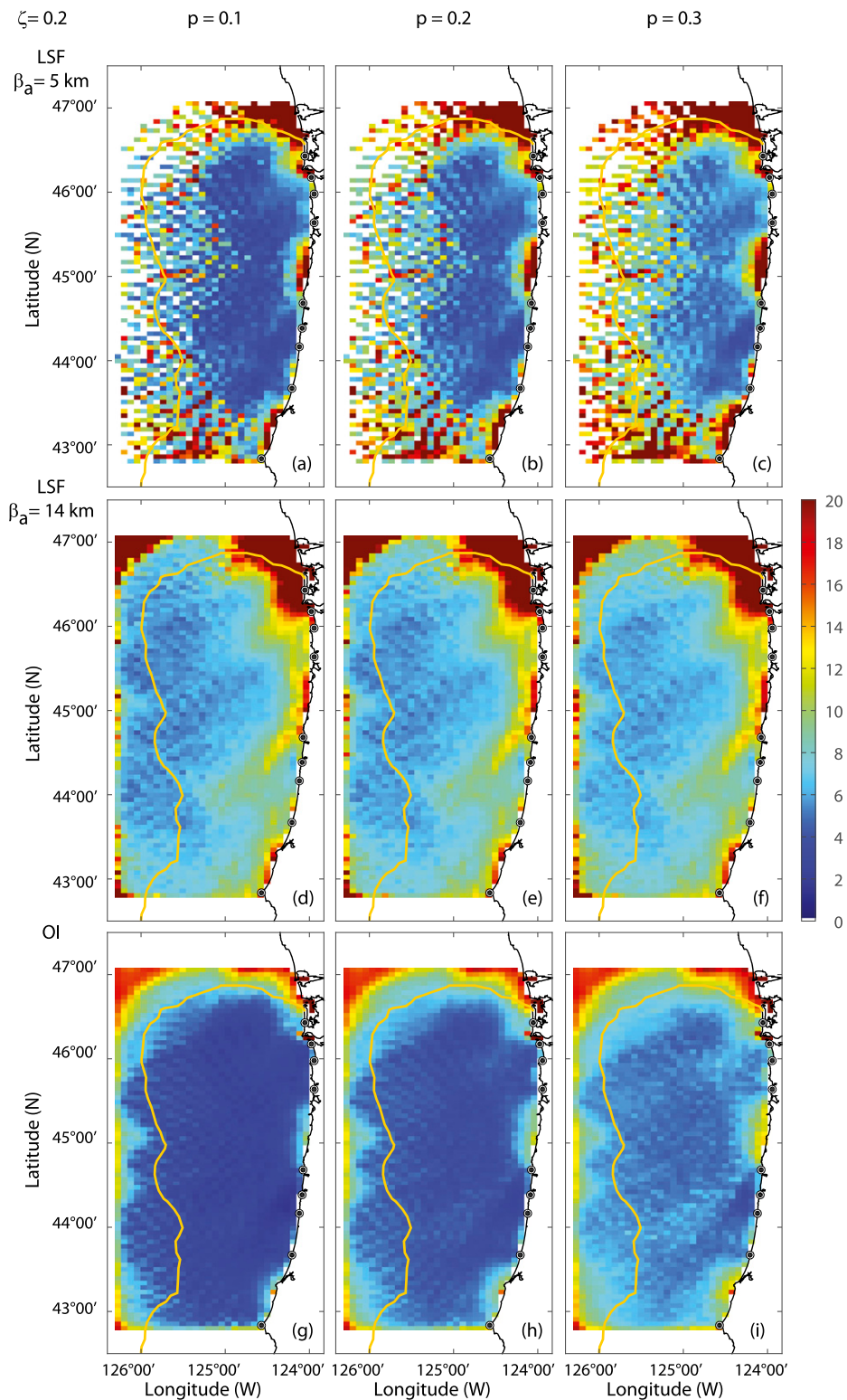


FIG. 13. Standard deviation (ξ ; cm s^{-1}) of the misfit between the estimated (LSF- and OI-mapped) and true vector currents as a function of an observational noise level (p) under 20% missing data ($\zeta = 0.2$). All vector current maps are estimated on a grid having a 6-km spatial spacing ($\Delta l = 6$ km). (top) LSF-mapped vector current fields ($\beta_a = 5$ km). (middle) LSF-mapped vector current fields ($\beta_a = 14$ km). (bottom) OI-mapped vector current fields. (a),(d),(g) $p = 0.1$. (b),(e),(h) $p = 0.2$. (c),(f),(i) $p = 0.3$ (see Table 1 for the simulation parameters). A yellow contour in the individual figures indicates the effective spatial coverage of HFRs off the Oregon coast for a period of two years (2007–08).

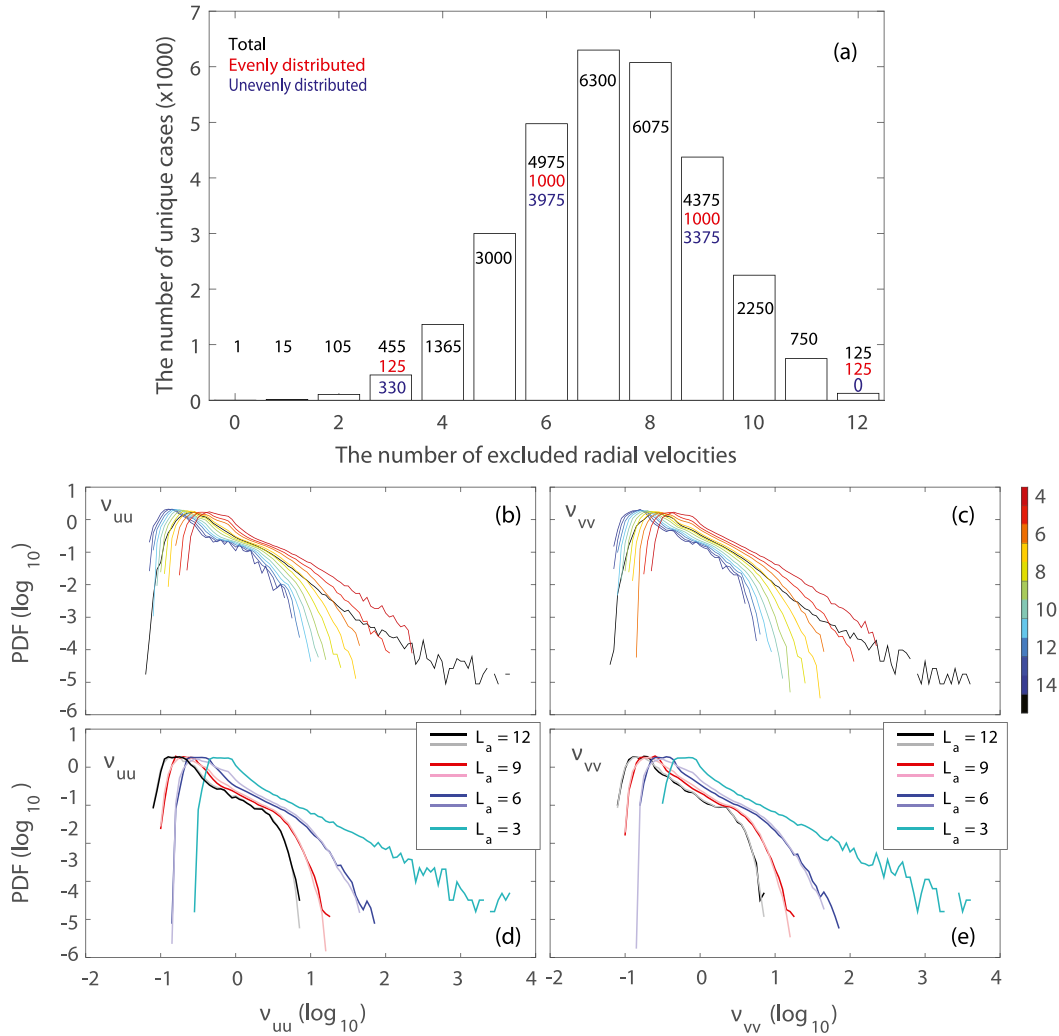


FIG. 14. The number of unique cases and uncertainties (or GDOPs) of vector currents (v_{uu} and v_{vv}) estimated using LSF under the evenly and unevenly distributed radial velocities within a search radius when 15 radial velocities ($L_a = 15$) are available from three radars ($K = 3$), and each radar contributes five radial velocities ($p_k = 5$; $k = 1, 2, \text{ and } 3$). At least single radial velocity from each radar should be contributed, and 5000 independent simulations are conducted for each case. (a) The number of unique cases as a function of the excluded number of the radial velocities within a search radius for uncertainty estimates. Evenly (red) and unevenly (blue) distributed cases are denoted. (b),(c) PDFs of uncertainty of vector currents (v_{uu} and v_{vv}) as a function of the total number of the radial velocities within a search radius; they share a color bar on the right. Black and colored curves denote the evenly ($L_a = 3, 6, 9, 12, \text{ and } 15$) and unevenly distributed cases, respectively. (d),(e) A comparison of PDFs of uncertainties (v_{uu} and v_{vv}) for the evenly (thick colors) and unevenly (paler colors) distributed cases for $L_a = 3, 6, 9, \text{ and } 12$.

errors in the realistic simulations based on the statistics of the observed radial velocity maps, which corresponds to the data quality and noise level, respectively.

1) SPACING FOR THE SPATIAL AND TEMPORAL SAMPLING OF THE RADIAL VELOCITIES

The azimuthal spacing and the number of the range bins are simulated as the operational HFRs within the study domain (e.g., 40 range bins and 5° azimuthal spacing). The range spacing depends on the operating (sweeping)

frequency of the radar. For instance, the pairs of typical operating (sweeping) frequency, given as 5 MHz (30 kHz), 13 MHz (60 kHz), and 25 MHz (150 kHz), correspond to the range spacings of 5, 2.5, and 1 km, respectively. Note that the HFRs off the Oregon coast have been operated at 5 MHz (25 kHz) and 13 MHz (75 kHz), which translate into 6- and 2-km range spacings, respectively. The effective radar viewing angle exhibits the geographic dependence of the HFR location relative to the shoreline. Specifically, based on the PDFs of the bearing angles of the

available radial solutions obtained from 10 HFRs off the coast of Oregon (Table 2), the viewing angle of the radars in this region covers from 180°T to 310°T from true north (not shown).

To observe the coastal oceanic variability from the low-frequency signals (e.g., seasonality) to the harmonics of the tides, an hourly sampling time interval is recommended, which corresponds to the Nyquist frequency of 12 cycles per day (cpd). The hourly radial velocity data are obtained from multiple signal processing, including averaging in time and space. Thus, the influence of the temporal averaging of the radial velocities on the variance of the observed currents (e.g., sinc function modulation because of boxcar averaging) is discussed in appendix C, which will be helpful for HFR users to configure a temporal averaging time window and to analyze the postprocessed data for scientific research.

Next, we define the polar coordinate grids for the individual radars, including the range and azimuthal spacing, and the bearing angle of the individual radars (Table 2). We sample the radial velocities on the polar coordinate grids from a true vector current field in the same way as conducted in section 2b.

2) IMPLEMENTATION OF THE MISSING DATA AND OBSERVATIONAL ERROR OF THE RADIAL VELOCITIES

Before we implement the missing data and observational noise in the true radial velocities obtained from the numerical model, we quantify these parameters in the observed radial velocities over a period of two years (2007–08) based on their temporal and spatial statistics.

The spatial correlations of the missing data, which were estimated using the covariance of the data replaced by ones for the missing data and zeros for the available observations show a minimal level of particular spatial structures (e.g., Gaussian or exponential function) or coherent structures in the range and azimuthal directions (first and second columns in Fig. 11). The spatial correlations of the radial velocities are consistent with the background surface circulation patterns across the sites (e.g., spatially uniform or long-term mean surface currents) because the white lines or areas where the zero correlations appear are orthogonal to the background currents (third and fourth columns in Fig. 11). In the radial velocity observations, the fraction of the missing data ranges from 20% to 40% depending on the locations (not shown). Thus, we generate the locations of the missing data in time and space as a random variable. Three cases of the data quality are simulated as the ratio ζ of the number of missing radial data to the total number of radial solutions, which are given as 0, 0.2, and 0.4 ($\zeta = 0, 0.2, \text{ and } 0.4$; see Table 1 for the simulation parameters). To evaluate the influence of the data quality, the vector

currents are estimated with the sampled radial velocity maps having zero observational noise ($p = 0$) (Fig. 12).

The observational error of the observed radial velocities is quantified as approximately 10 cm s^{-1} and is represented by 0.1765 ($p = \gamma^2/\sigma^2 = 0.1765$) because the minimum correlation is equal to -0.85 when the paired radial velocities are oppositely faced (e.g., Kim et al. 2008; Kim 2015):

$$\rho_{\min} = -\frac{\sigma^2}{\sigma^2 + \gamma^2} = -0.85, \quad (24)$$

based on the standard deviation of the sum of the nearby radial pairs obtained from multiple radars and their correlations (Fig. B2 in Yoo et al. 2017). We consider the observational error of the radial velocities as a sum of the sampling error and measurement error. To evaluate the influence of the noise level, the radial velocity maps with a constant level of missing data ($\zeta = 0.2$) and varying noise levels of 0.1, 0.2, and 0.3 ($p = 0.1, 0.2, \text{ and } 0.3$; see Table 1 for the simulation parameters) are simulated (Fig. 13).

c. Spatial mapping of radial velocities and associated uncertainty

Regarding the choice of the parameters in the vector current estimates using LSF and OI, two search radii in LSF are chosen as 1) 5 km to avoid potential oversampling of the surface currents and to set it less than the spacing of the rectangular grid ($\beta_a = 5 \text{ km}$) and 2) 14 km to simulate the operational system ($\beta_a = 14 \text{ km}$). In OI, the parameters are chosen as an isotropic exponential function with decorrelation length scales (λ_x and λ_y) of 10 km in the x and y directions; signal (σ^2) and noise (γ^2) variance of 1600 and $40 \text{ cm}^2 \text{ s}^{-2}$, respectively; and a search radius of 15 km, where the correlations are effectively reduced [$\beta_b = 14 \text{ km}$ when $\rho_0 = 0.25$; see Kim et al. (2008) and appendix D for more details] (see Table 1 for the other simulation parameters). Note that the correlation function can be assumed to be anisotropic depending on the principal component of the regional circulation. Although a search radius is not required in OI, it is proposed to minimize the calculation time because the size of the inverting matrix (cov_{da}) depends on the number of radial velocities L_b within the search radius. An exponential function is chosen as the correlation function to set a lower level of spatial smoothing than that of the Gaussian correlation function. The influence of the decorrelation length scales is insignificant if they are longer than the size of the rectangular grid.

The spacing of the rectangular grid is proposed as 6 km ($\Delta l = 6 \text{ km}$) in consideration of the minimum

resolution of the true vector current fields ($\Delta x = 2$ km) and the simplicity of the performance evaluation for the entire Oregon coast, although a high-resolution grid spacing ($\Delta l = 2$ km) is possible for 13-MHz radar sites (STV, SEA, YHS, WLD, and WSH; see Table 2 for full station and regional names of radar sites).

d. Evaluation

1) OVERVIEW

Although we evaluate the performance of reconstruction in the idealized simulations with the ensemble-averaged misfit and uncertainty (section 2d), in the realistic simulations, we chose the standard deviation [ξ in Eq. (25)] of the misfit to quantify the difference between the estimates and true values and to present the results more effectively,

$$\xi(\mathbf{x}) = \sqrt{\langle \mathbf{u}_e^2(\mathbf{x}, t) \rangle}. \tag{25}$$

As described above, the four parameters [δ , Δs , $\Delta \theta$, and Δl in Eqs. (21) and (22); Table 1] are predetermined in the realistic simulations. Thus, the performance of the reconstruction is evaluated in terms of a search radius in LSF (β_a), data quality (ζ), and noise level (p) (Figs. 12 and 13; Table 1).

2) INFLUENCE OF SEARCH RADIUS, DATA QUALITY, AND NOISE LEVEL

A longer search radius in LSF yields a higher standard deviation of the misfit (Figs. 12a–f and 13a–f) because the estimated vector current fields can be smooth and may not resolve fine flow structures (e.g., submesoscale and below). Similarly, the enhanced magnitudes of the misfit tend to appear in the boundaries of the domain and the areas near the baselines under the longer search radius. However, the effective spatial coverage of the estimated vector currents becomes larger under the longer search radius (Figs. 12a–f and 13a–f).

As the amount of missing data in the radial velocity maps increases, the standard deviation of the misfit increases at the edge of the domain, in particular, and the effective spatial coverage shrinks more significantly in the LSF-mapped vector current fields than in the OI-mapped ones (Figs. 12a–c and 12g–i). As the noise level increases, the standard deviation of the misfit increases slightly and the effective spatial coverage is nearly identical (Fig. 13). The influence of the missing data on the estimated vector currents is more dominant than that of the observational error (Figs. 12 and 13).

3) SUMMARY

The standard deviation of the misfit of vector currents estimated with the two inverse methods (LSF and OI)

and different search radii in LSF ($\beta_a = 5$ and 14 km) is summarized as follows:

$$\xi_{OI} < \xi_{LSF,5km} < \xi_{LSF,14km}. \tag{26}$$

For better observations of the surface currents using the operational HFRs, we recommend using a decorrelation length scale of less than 2 times the grid spacing of the vector currents in OI and a search radius of less than the grid spacing of the vector currents in LSF to minimize the spatial smoothing. Because the observational noise level is less influential in the performance of the reconstruction of the surface current fields than the density of the missing data, it can be a priority to obtain the complete radial velocity maps. In addition, the number of the radial velocities within the given search radius is recommended as less than 10 in LSF and 5–20 in OI (Fig. 2a), which can constrain the distance between the radars under several combinations of the available operating and sweeping frequencies. Above all, the choice of the parameters should be based on the primary spatial scales of the surface currents of interest.

4. Discussion

a. Dependence of the distribution of the radial velocities on the uncertainty

We examine how the uncertainties (or GDOPs) of the LSF-mapped vector currents depends on cases in which the radial velocities within a search radius involving multiple radars are evenly and unevenly distributed, assuming that the L_a total radial velocities within a search radius are available from K individual radars and each radar contributes between at least one and q_k radial velocities ($q_k \geq 1$; $k = 1, 2, \dots, K$; $L_a = \sum_k q_k$). For example, three radars contribute a maximum of 15 radial velocities within a search radius, that is, five radial velocities from each radar ($K = 3$ and $L_a = 15$). All radial velocities have unique bearing angles with a resolution of 1° , and the bearing angles from a single radar have an interval of 5° because they are assumed to be continuously sampled in a polar coordinate grid. Figure 14a shows the total number of the unique combinations of the radial velocities ($N = 27\,791$) as a function of the excluded number of the radial velocities from the total number of the radial velocities in a systematic way, which is calculated as follows:

$$N = \sum_{l=0}^{L_a-3} \binom{L_a}{l}, \tag{27}$$

and the number of the evenly (red) and unevenly (blue) distributed cases is marked only for $L_a = 3, 6, 9, 12$, and 15. The PDFs of the estimated uncertainty (ν_{uu} and ν_{vv}) are presented as a function of the total number of the

participating radial velocities with a distinction of the evenly distributed cases with black ($L_a = 3, 6, 9, 12,$ and 15) and the unevenly distributed cases with colors (Figs. 14b and 14c). Although the evenly distributed cases may have less uncertainty, the uncertainty of the LSF-mapped vector currents highly depends on the number of the radial velocities instead of the degrees of their distribution. Additionally, the uncertainties estimated from the evenly and unevenly distributed cases for $L_a = 3, 6, 9,$ and 12 did not show that much difference in their PDFs (Figs. 14d and 14e). Thus, we conclude that the degree of the distribution of the radial velocities within the search radius does not affect the GDOP of the estimated vector currents.

b. Scientific descriptions on “sufficient” information to resolve an orthogonal vector current field

We have examined whether the nonorthogonally and irregularly sampled scalar velocity data contain sufficient information to reconstruct the true vector current field. The HFR-derived radial velocity maps and altimeter-derived along-track SSHs exhibit similarity in terms of the nature of nonorthogonally and irregularly sampled raw data to the vector current mapping. Considering both observations using the HFRs and altimeters on the same coastal area within 100 km from the coast, the surface current measurements using the HFRs have relatively denser and more abundant spatial samples than the altimeter-derived SSH observations to resolve the orthogonal vector current maps having designated resolutions (e.g., Wilkin et al. 2002; Kuragano et al. 2015). Although the performance of the reconstruction from the given nonorthogonally and irregularly sampled scalar data may depend on 1) the data quality associated with the missing data, 2) the observational noise level in the observed radial velocities, and 3) the chosen inverse methods (e.g., LSF or OI), the standard deviation of the misfit between the estimates and true values ranges from 2 to 10 cm s^{-1} in the center of the domain and increases at the edge of the domain and areas close to the baselines, based on simulations using the HFRs off the Oregon coast. Thus, the HFR-derived radial velocity maps contain sufficient information to reconstruct the vector current field.

c. Propagations of the observational error of the radial velocities

The observational error of the radial velocities, which is quantified with long-term observations of the paired radial velocities, is input into the OI mapping machine as the mapping error (a regularization term of the converting matrix) and comes out as the normalized uncertainty of the vector currents, which contain the

directional uncertainty as part of systematic error. However, because LSF assumes an infinite SNR, the mapping error is assumed to be very small or zero when it is formulated, and the GDOP is considered as the uncertainty of the vector currents (e.g., Kim et al. 2008). In the application of the vector currents, the uncertainty of the vector currents can propagate through the final outcomes. For example, in the forward and backward time integrations of the consecutive vector current maps, the uncertainty of the vector currents can be incorporated as a random variable (e.g., Ullman et al. 2006; Kim et al. 2009; Rogowski et al. 2015),

$$\mathbf{x}(t_N) = \mathbf{x}(t_0) + \sum_{j=1}^N [\mathbf{u}(\mathbf{x}, t_j) + \epsilon_e(\mathbf{x}, t_j)] \Delta t, \quad (28)$$

where \mathbf{x} , t_0 , and Δt denote the horizontal position of the Lagrangian trajectory, initial time, and time interval, respectively.

d. Potential applications in coastal oceanography using the proposed analysis

The proposed analysis is applicable to evaluate the optimal installation locations of the radar to best observe the regional surface circulation. Because a radial velocity is a cosine projection of the bearing angle of the radar on the true current field, a mistakenly situated radar may not report the dominant surface circulation effectively. Thus, the regional numerical model outputs can be used as a resource to evaluate the potential locations of the radar. The constellation of the radars and associated GDOPs can be parameters to optimize the cost function of an effective observing system using HFRs on the regional surface circulation. These findings can be used to develop relevant techniques, such as the detection of eddies and fronts, configuration of HFR installation locations to achieve appropriate spatial coverage, and accuracy evaluations of the HFR observations. Additionally, the sensitivity resulting from the errors of the directional solutions can be investigated by applying an opposite sign of the radial velocities or by misplacing the radial velocity data randomly, which can simulate the radial solutions that are mistakenly calculated from the direction-finding algorithms. However, coastal shadowing and regional noise resulting from the environmental condition of the radar signals may represent additional factors that can alter the performance of the surface current observations using the HFRs. Note that the limitations of obtaining permission to use the desired coastal real estate for scientific measurements and of providing power and Internet communications to a chosen site are additional constraints to consider. When waterborne pollutants in marine accidents and

larvae in marine protected areas are tracked as a part of passive tracer dispersion studies, the proposed analysis may report the uncertainty of their locations.

5. Conclusions

We evaluated how well an orthogonal two-dimensional vector field can be reconstructed from a set of non-orthogonally and irregularly sampled scalar velocity data as an analogy of the HFR-derived surface radial velocity maps and their mapping to a vector current map. We generated the radial velocity maps by sampling two-dimensional surface vector currents, obtained from a simple spectral model and a regional numerical simulation, on the polar or elliptical coordinator grid points as configured in the operational HFRs. Then, the radial velocity maps were combined into a vector current field using inverse methods: unweighted least squares fitting and optimal interpolation. The true and estimated vector currents were evaluated with 1) the simulation parameters built into the simple spectral model and 2) the degrees of the quality and observational error of the radial velocities associated with simulated missing data and noise level, respectively. A greater number of missing data and higher observational errors correspond to an increase in the standard deviation of the misfit and a significant reduction in the effective spatial coverage of the estimated vector current fields. Although the reconstruction performance depends on the chosen inverse methods and parameters, the nonorthogonally and irregularly sampled radial velocities contain sufficient information to reconstruct the given vector current field. This paper will provide technical details for resolving a vector current field and guidelines for the practical design of the spatial sampling of the current field using the HFRs.

Acknowledgments. Hyun Sup Soh and Sung Yong Kim are supported by grants through the Basic Science Research Program through the National Research Foundation (NRF), Ministry of Education (NRF-2017R1D1A1B03028285); “Research for Applications of Geostationary Ocean Color Imager” via the Korea Institute of Marine Science and Technology Promotion (KIMST), Ministry of Oceans and Fisheries; and the Disaster and Safety Management Institute, Ministry of Public Safety and Security (KCG-01-2017-05), South Korea. Special thanks are given to Dudley Chelton at Oregon State University who brought up a question on the HFR observations and provided valuable discussion. This work is a part of the graduate studies of the first author. The MATLAB scripts for simulated velocity fields in the one-dimensional and two-dimensional domains are available upon request to the corresponding author.

APPENDIX A

Does a Single Radial Velocity Map Contain Sufficient Information to Reconstruct an Orthogonal Vector Current Field?

Extracting a vector current map from a single HFR-derived radial velocity map has been investigated with several studies using an assumption of nondivergent flows, spatial averaging of radial velocity maps, and covariance statistics of a single radar velocity data (e.g., Bjorkstedt and Roughgarden 1997; Liu et al. 2007; G. Voulgaris et al. 2010, 10th International Radiowave Oceanography Workshop (ROW-10) presentation; Hickey 2010; Barrick 2003; Voulgaris et al. 2011). However, these approaches have been evaluated in the present study, and none of them could retrieve the true vector current field correctly. These heuristic lessons will be beneficial to the HFR users who may try to apply similar approaches and assumptions.

a. True vector current fields

We use a simple model and a spectral model to generate the vector current maps and radial velocity maps and to evaluate the approaches to extract the vector current map from a single radial velocity map.

1) A SIMPLE MODEL

The vector current fields are simply simulated with the spatially uniform currents and directional shear currents,

$$u(x, y) = \frac{u_M - u_m}{L_y} y + \epsilon_u(x, y) \quad \text{and} \quad (\text{A1})$$

$$v(x, y) = \frac{v_M - v_m}{L_x} x + \epsilon_v(x, y), \quad (\text{A2})$$

where L_x and L_y are the size of the domain in the x and y directions, respectively, and u_M and v_M and u_m and v_m are the velocity components at the edge of the domain, which can have the same values or maximum and minimum depending on the degrees of shear and uniform flows.

The vector current fields with a single eddy, including closed, inward, and outward spirals, are formulated with

$$u(x, y) = u_r w \cos \theta + u_\theta w \sin \theta + \epsilon_u(x, y) \quad \text{and} \quad (\text{A3})$$

$$v(x, y) = -u_\theta w \cos \theta + u_r w \sin \theta + \epsilon_v(x, y), \quad (\text{A4})$$

where u_r and u_θ are the velocity components in the radial and azimuthal directions, respectively;

$$w = \frac{a}{\pi} \frac{r}{2s^2} \exp\left(-\frac{r^2}{2s^2}\right), \quad (\text{A5})$$

$$r = \sqrt{(x - x_0)^2 + (y - y_0)^2}, \quad (\text{A6})$$

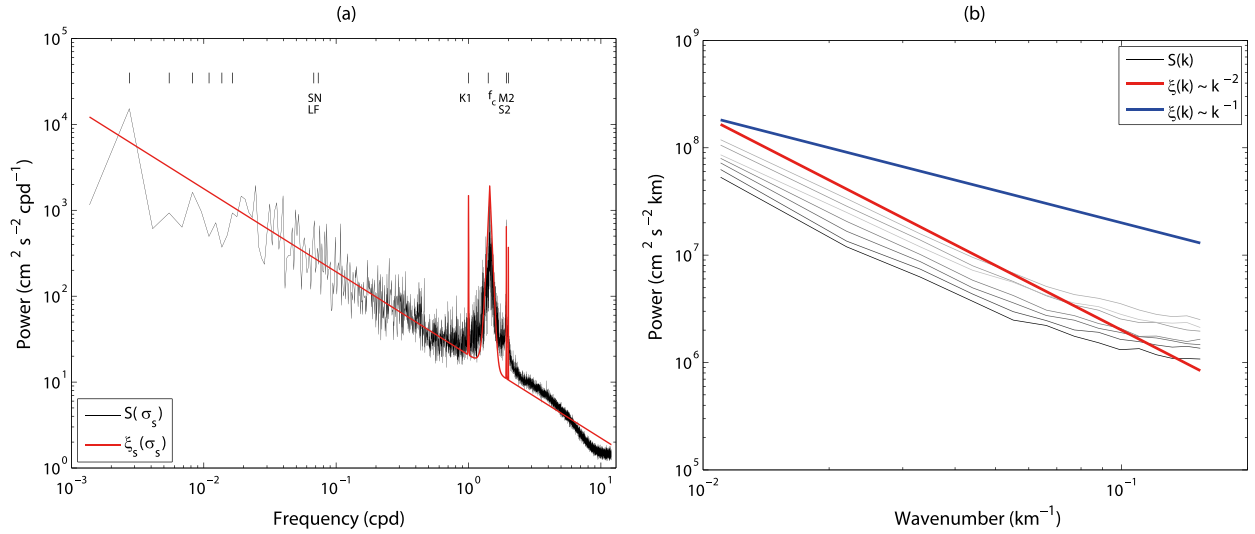


FIG. A1. (a) A spatially averaged frequency-domain energy spectrum [$S(\sigma_s)$] of hourly radial velocities at MAN1 (Table 2 and Figs. 11a–d) at 225 grid points more than 80% temporal data availability over a period of two years (2007–08). Barotropic tides (K_1 , M_2 , and S_2), inertial frequency (f_c), spring–neap (SN; 14.765 days), and lunar fortnightly (LF; 13.661 days) tides, along with the seasonal cycle and its five harmonics (SA_1 , SA_2 , . . . , SA_6) are marked. An approximated energy spectrum [$\xi(\sigma_s)$, red curve] of the hourly radial velocities in the frequency domain is overlaid. (b) Wavenumber energy spectra [$S(k)$, gray curves] of the hourly radial velocities in the range direction at individual azimuthal angles, and their reference decay slopes of k^{-1} and k^{-2} (blue and red lines, respectively).

$$\epsilon_u = \gamma \langle u^2 \rangle^{1/2} \mathbf{N}(0, 1), \quad \text{and} \quad (\text{A7})$$

$$\epsilon_v = \gamma \langle v^2 \rangle^{1/2} \mathbf{N}(0, 1), \quad (\text{A8})$$

where s denotes the scale of eddies; x_0 and y_0 denote the center of the eddy; and a indicates the amplitude of the eddy (clockwise if $a < 0$ and counterclockwise if $a > 0$). For all cases of the uniform, shear, and vortical flow fields [Eqs. (A1)–(A4)],

an observational noise can be simulated with a Gaussian random variable, which can be assumed as the ratio γ of noise variance to signal variance. The angle brackets in Eqs. (A7) and (A8) denote the spatial mean.

2) A SPECTRAL MODEL

The vector current fields are defined as

$$u(x, y, t) = \sum_{m=-M^*}^{M^*} \sum_{n=-N^*}^{N^*} \sum_{s=-S^*}^{S^*} \hat{A}_{mns} \cos \vartheta_{mns} + \hat{B}_{mns} \sin \vartheta_{mns} \quad \text{and} \quad (\text{A9})$$

$$v(x, y, t) = \sum_{m=-M^*}^{M^*} \sum_{n=-N^*}^{N^*} \sum_{s=-S^*}^{S^*} \hat{C}_{mns} \cos \vartheta_{mns} + \hat{D}_{mns} \sin \vartheta_{mns}, \quad (\text{A10})$$

where

$$\vartheta_{mns} = k_m x + l_n y - 2\pi \sigma_s t = 2\pi \left(\frac{m}{L_x} x + \frac{n}{L_y} y \right) - 2\pi \sigma_s t, \quad (\text{A11})$$

k_m and l_n denote the wavenumber, L_x and L_y are the length of the domain in the x and y directions, respectively, and σ_s indicates the frequency (cpd). As the spatial covariance in the physical space is equivalent to the power spectrum in the wavenumber domain (e.g., Cohen 1992; Brigham 1988), the coefficients (\hat{A}_{mn} , \hat{B}_{mn} , \hat{C}_{mn} , and \hat{D}_{mn}) are assumed to be random

variables of normal distribution with zero mean and unit standard deviation [$\mathbf{N}(0, 1)$], for instance,

$$\hat{A}_{mns} = (\xi_{mn})^{1/2} (\xi_s)^{1/2} \mathbf{N}(0, 1), \quad (\text{A12})$$

with the power spectrum of the vector current fields in the wavenumber [$\xi_{mn} = \xi(k_m, l_n)$] and frequency [$\xi_s = \xi(\sigma_s)$]

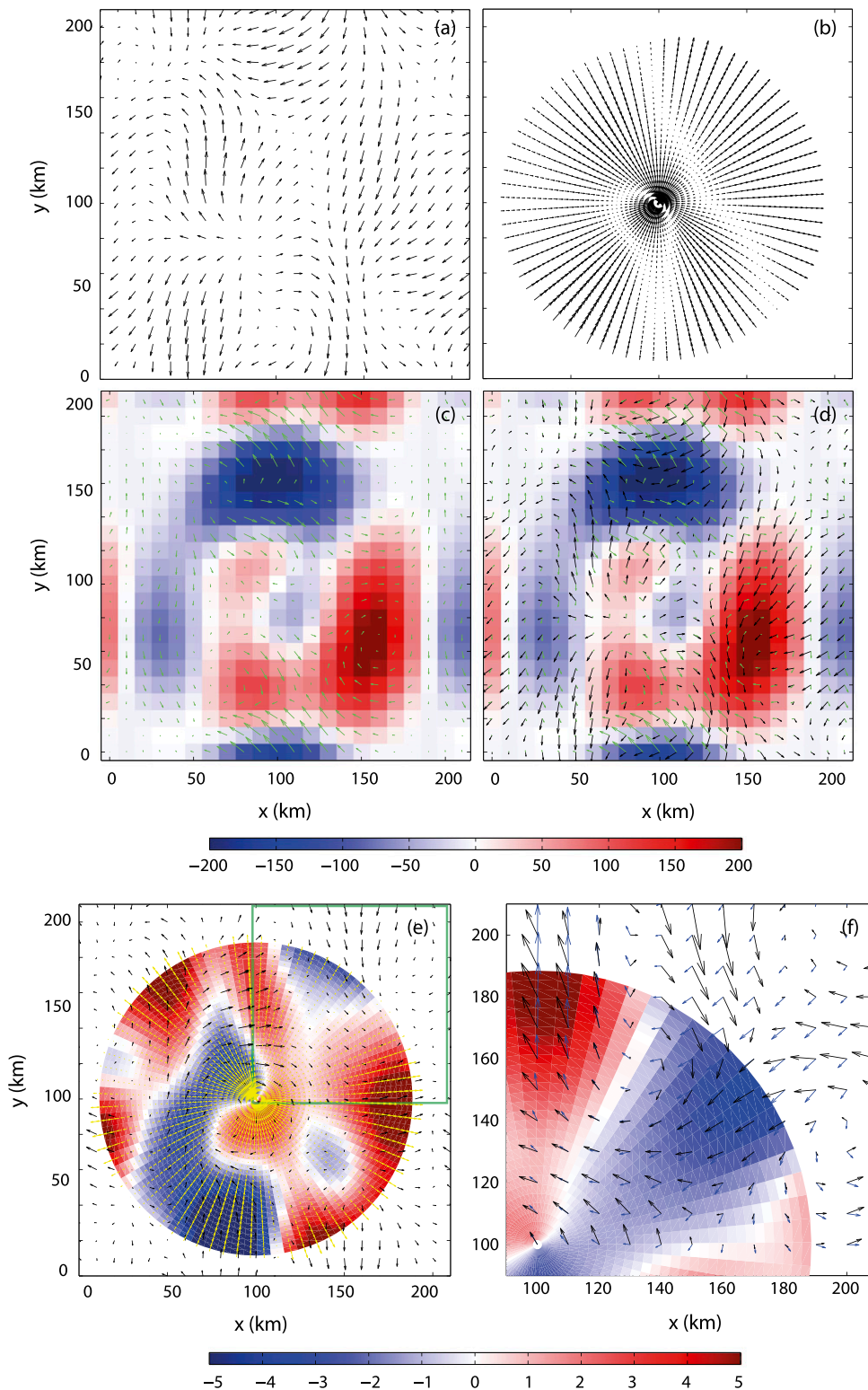


FIG. A2. (a),(b) An example of the true (or model) vector current field based on a spectral model and its radial velocity map sampled from a single radar located at the center of the domain. (c) An example of the estimated vector current field using an assumption of the horizontally nondivergent flow. Clockwise (blue) and counterclockwise (red) streamfunctions ($\text{cm}^2 \text{s}^{-1}$). (d) A comparison between the OI-mapped (cyan) and true (black) vector current fields. (e) An example of the true (or model) vector currents (black arrows) and corresponding radial velocities [yellow arrows or red (positive) and blue (negative); cm s^{-1}]. (f) An example of the true (black) and estimated vector currents (blue) based on the sample covariance matrix [a close-up view of the green box in (e)].

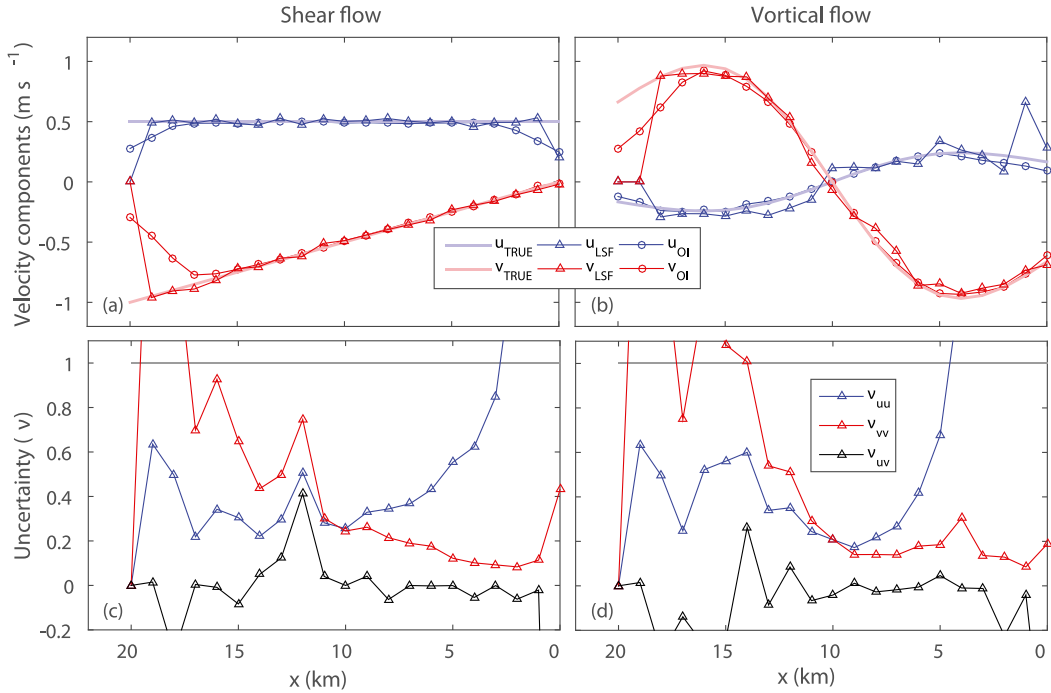


FIG. B1. (a),(b) Estimated vector current components (u and v ; m s^{-1}) along a cross-shore line (green lines in Figs. 1a and 1b) using LSF and OI under the same parameters in Fig. 1 but with the search radius of 1.5 km in LSF ($\beta_a = 1.5$ km). (c),(d) GDOPs [v for LSF; Eq. (5)] (see Table 1 for the simulation parameters).

domains. The wavenumber spectrum is approximated with a two-dimensional Gaussian or exponential function, respectively:

$$\xi(k_m, l_n) = 4\pi\lambda_x\lambda_y \exp(-k_m^2\lambda_x^2 - l_n^2\lambda_y^2) \quad \text{or} \quad (\text{A13})$$

$$\xi(k_m, l_n) = \frac{2\pi\lambda_x\lambda_y}{(1 + k_m^2\lambda_x^2 + l_n^2\lambda_y^2)^{3/2}}, \quad (\text{A14})$$

and λ_x and λ_y denote the decorrelation length scales in the x and y directions, respectively.

Conversely, the spectrum in the frequency domain of the vector current time series is approximated with the background energy and variances at the peak frequencies,

$$\xi(\sigma_s) = A\sigma_s^{-\alpha} + \sum_{l=1}^L B_l \exp\left[-\frac{|\sigma_s - \nu_l|}{(\lambda_l)_l}\right], \quad (\text{A15})$$

where A and B_l are the amplitudes of the spectra in the frequency domain, α is the slope of the background energy, and ν_l and $(\lambda_l)_l$ denote the frequencies with peaks and their bandwidths, respectively ($l = 1, 2, \dots, L$). The bandwidth is determined by the width to have b decibels reduced from the peak, where b is equal to 1, 5, or 10 depending on the decay pattern of the local peak.

In this work the energy spectra of the radial velocities in the wavenumber and frequency domains are approximated with Eqs. (A14) and (A15), respectively.

The one-dimensional wavenumber spectra estimated in the range direction (the outward direction from the center of the radar is the positive range axis) have a slope of k^{-2} ; thus, the exponential wavenumber spectrum is applied (Fig. A1a). The spatially averaged energy spectrum of the radial velocity time series in the frequency domain contains two peaks at the inertial frequency (≈ 1.42 cpd) and K_1 frequency (1.0027 cpd) along with the background energy of the red spectrum (Fig. A1b). The coefficients in Eq. (A15) are estimated as $A = 54.8$, $\alpha = 1.1062$, $B_1 = 630.95$, and $\lambda_l = 0.01$ at the inertial frequency, and $B_2 = 316.22$ and $\lambda_l = 0.08$ at the K_1 frequency.

b. Extracting vector currents

1) HORIZONTALLY NONDIVERGENT FLOWS

The vector current fields are assumed to be the horizontally nondivergent flow to satisfy the geostrophic balance (e.g., Liu et al. 2007; Bjorkstedt and Roughgarden 1997),

$$\frac{\partial u}{\partial x} + \frac{\partial v}{\partial y} = 0. \quad (\text{A16})$$

The streamfunction ψ is decomposed with normal modes in the x and y directions,

$$\psi = \sum_{m=-M}^M \sum_{n=-N}^N A_{mn} \cos \nu_{mn} + B_{mn} \sin \nu_{mn}, \quad (\text{A17})$$

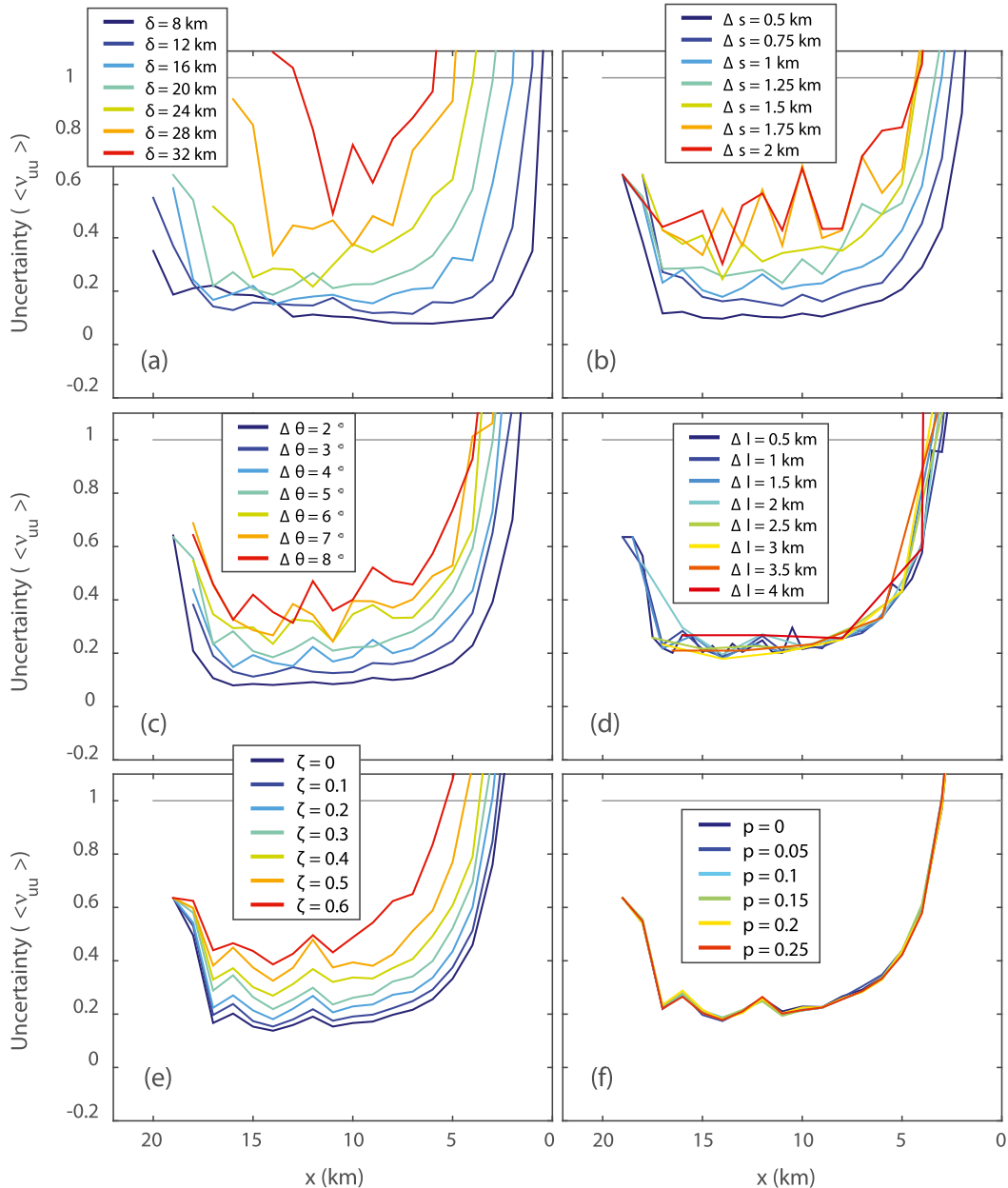


FIG. B2. Ensemble-averaged GDOPs ($\langle v_{uu} \rangle$) of the LSF-mapped u component estimated from the radial velocity maps (Fig. 1b) are evaluated with the (a) separation distance ($\delta = 8, 12, 16, 20, 24, 28,$ and 32 km), (b) range spacing ($\Delta s = 0.5, 0.75, 1, 1.25, 1.5, 1.75,$ and 2 km), (c) azimuthal spacing ($\Delta \theta = 2^\circ, 3^\circ, 4^\circ, 5^\circ, 6^\circ, 7^\circ,$ and 8°), (d) spacing of the rectangular grid ($\Delta l = 0.5, 1, 1.5, 2, 2.5, 3, 3.5,$ and 4 km), (e) data quality ($\zeta = 0, 0.1, 0.2, 0.3, 0.4, 0.5,$ and 0.6), and (f) noise level ($p = 0, 0.05, 0.1, 0.15, 0.2,$ and 0.25) under the search radius of 1.5 km ($\beta_a = 1.5$ km). Simulations are conducted with combinations of a single parameter with discretely changing values and the rest of the parameters with a fixed value for the control simulations (see Table 1 for the simulation parameters).

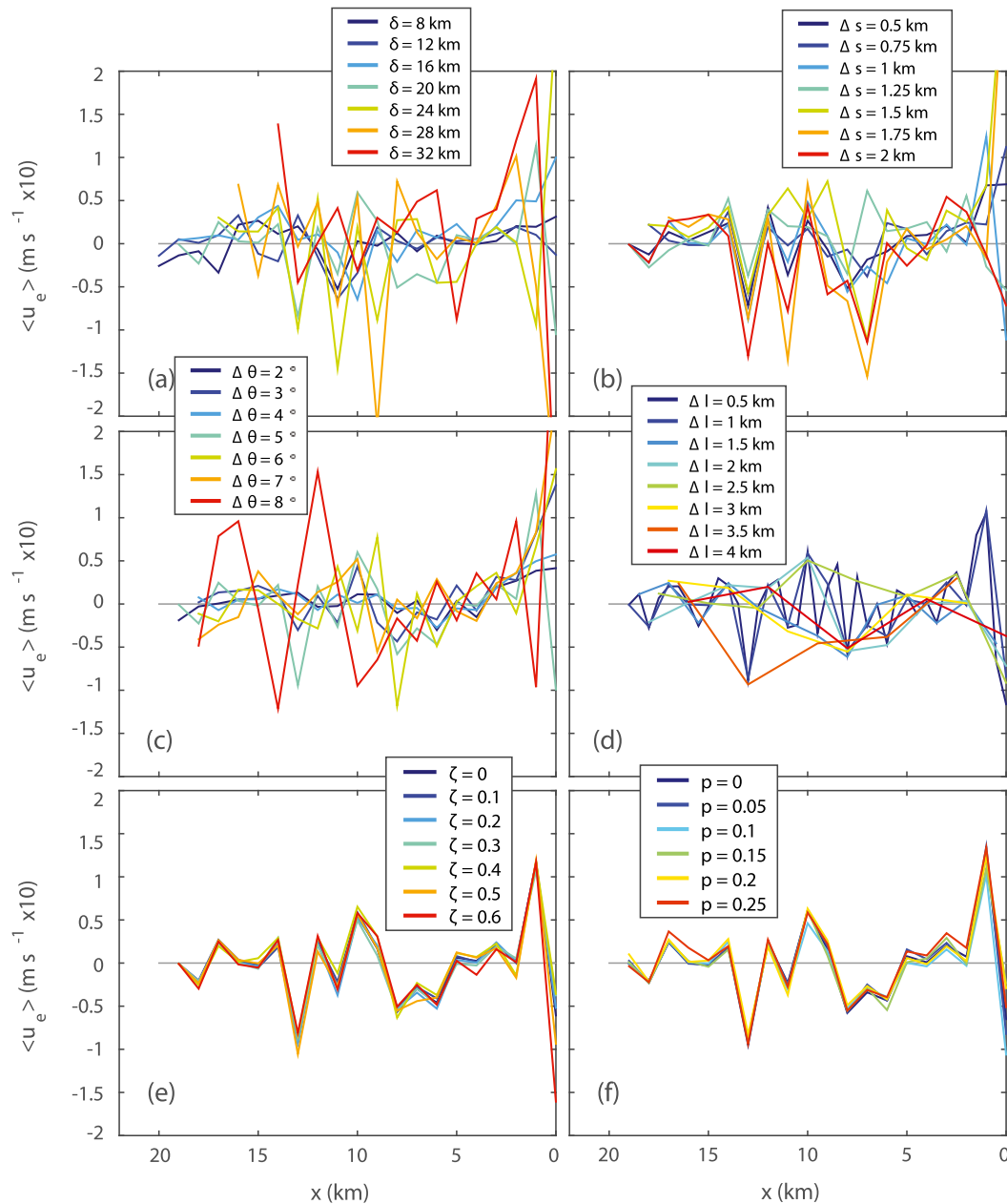


FIG. B3. Ensemble-averaged misfits ($\langle u_e \rangle \times 10; \text{m s}^{-1}$) of the LSF-mapped u component estimated from the radial velocity maps (Fig. 1b) are evaluated with the (a) separation distance ($\delta = 8, 12, 16, 20, 24, 28,$ and 32 km), (b) range spacing ($\Delta s = 0.5, 0.75, 1, 1.25, 1.5, 1.75,$ and 2 km), (c) azimuthal spacing ($\Delta \theta = 2^\circ, 3^\circ, 4^\circ, 5^\circ, 6^\circ, 7^\circ,$ and 8°), (d) spacing of the rectangular grid ($\Delta l = 0.5, 1, 1.5, 2, 2.5, 3, 3.5,$ and 4 km), (e) data quality ($\zeta = 0, 0.1, 0.2, 0.3, 0.4, 0.5,$ and 0.6), and (f) noise level ($p = 0, 0.05, 0.1, 0.15, 0.2,$ and 0.25) under the search radius of 1.5 km ($\beta_a = 1.5$ km). Simulations are conducted with combinations of a single parameter with discretely changing values and the rest of the parameters with a fixed value for the control simulations (see Table 1 for the simulation parameters).

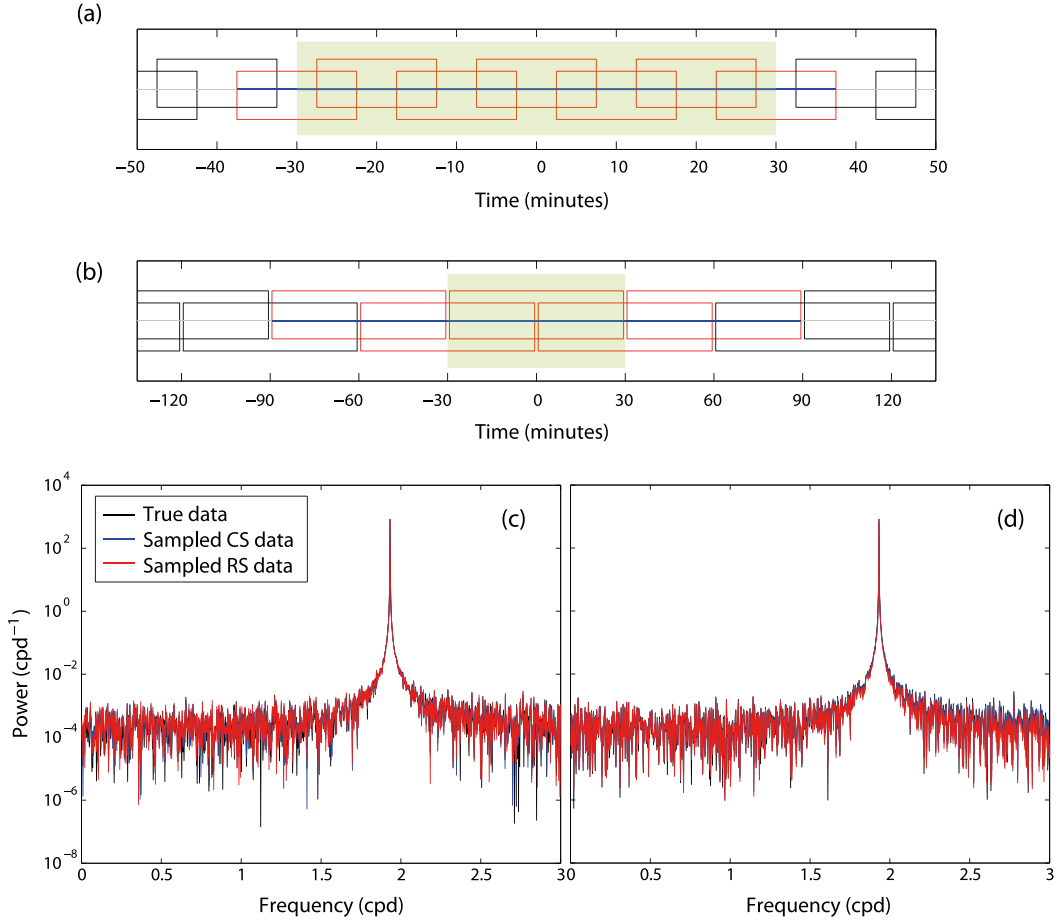


FIG. C1. (a),(b) A schematic diagram of the averaging time window in the operational SeaSonde short- and long-range compact array systems. A single cross-spectra (CS) file, reported every 10 min in the short-range system (every 30 min in the long-range system), is generated from observations within a 15-min-long (60-min-long) time window (red boxes). A single radial velocity (RS) solution, reported every 60 min for both systems, is generated by the cross-spectra files within a 75-min-long (180-min-long) time window (thick blue horizontal lines). Based on the effective time window for the hourly radial velocity data, the data outside of green boxes are overlapped with the data within an adjacent effective time window, i.e., a period of 15 min over 75 min (120 min over 180 min) is overlapped. Note that the time windows are slightly shifted to avoid their overlapping in (b). (c),(d) Power spectra of a pure M_2 time series (black) with a white noise (e.g., 10% of signal variance) for a period of 2 months and the boxcar-averaged time series as the cross-spectra (blue) data and radial velocity (red) are sampled.

and the corresponding current components (u and v) are

$$u = -\frac{\partial\psi}{\partial y} \tag{A18}$$

$$= \sum_{m=-M}^M \sum_{n=-N}^N A_{mn} l_n \sin\nu_{mn} - B_{mn} l_n \cos\nu_{mn} \quad \text{and} \tag{A19}$$

$$v = \frac{\partial\psi}{\partial x} \tag{A20}$$

$$= \sum_{m=-M}^M \sum_{n=-N}^N -A_{mn} k_m \sin\nu_{mn} + B_{mn} k_m \cos\nu_{mn}, \tag{A21}$$

where $\nu_{mn} = k_m x + l_n y$.

The radial velocity at a given azimuthal and range bin [Eq. (2)] is expressed with the normal modes and their coefficients,

$$r = \sin\nu_{mn} (l_n \cos\theta - k_m \sin\theta) A_{mn} + \cos\nu_{mn} (-l_n \cos\theta + k_m \sin\theta) B_{mn}. \tag{A22}$$

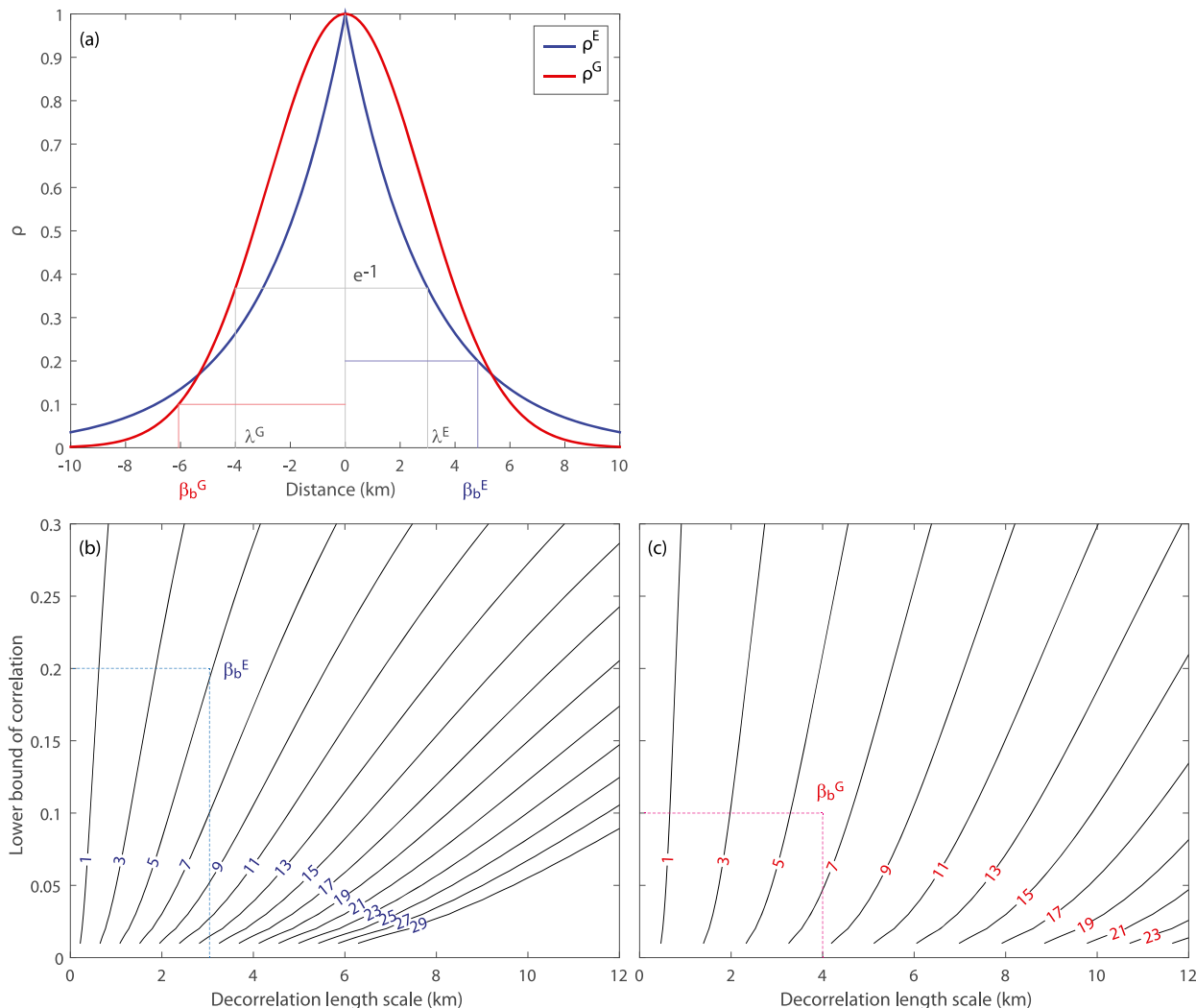


FIG. D1. (a) A schematic diagram to show search radii (β_b^E when $\rho_0 = 0.1$ and β_b^G when $\rho_0 = 0.2$) in OI under a given decorrelation length scale (λ^E and λ^G when $\rho_0 = e^{-1}$) and a lower bound of the correlation ($\rho_0 = 0.1$ or $\rho_0 = 0.2$) for one-dimensional exponential (ρ^E) and Gaussian (ρ^G) correlation functions. A search radius (β_b) is determined by the decorrelation length scale and the lower bound of the correlation: (b) an exponential correlation function and (c) a Gaussian correlation function.

The inverse method is applied to estimate A_{mm} and B_{mm} (e.g., Wunsch 1996). The vector currents estimated under the assumption of nondivergent flow are not consistent with the true currents (Fig. A2). Although this approach is evaluated by changing the number of modes [Eq. (A17)] and the SNR in the inverse method, the estimated vector current fields are quite different from the true vector current fields.

2) OBJECTIVE MAPPING USING DATA COVARIANCE MATRICES

The data covariance of the radial velocities is used as a constraint to estimate the vector current maps (e.g., Kim et al. 2007). The objective mapping using data covariance is conducted as follows:

$$\hat{\mathbf{u}} = \text{cov}_{\text{dm}}^\dagger \text{cov}_{\text{dd}}^{-1} \mathbf{r}, \tag{A23}$$

where cov_{dm} is the covariance between model radial velocities [Eq. (A22)] and model vector currents ($\mathbf{u} = [u \ v]^\dagger$),

$$\text{cov}_{\text{dm}} = \langle \mathbf{r} \mathbf{u}^\dagger \rangle, \tag{A24}$$

cov_{dd} is the covariance between model vector currents,

$$\text{cov}_{\text{dd}} = \langle \mathbf{r} \mathbf{r}^\dagger \rangle + \langle \boldsymbol{\epsilon} \boldsymbol{\epsilon}^\dagger \rangle, \tag{A25}$$

and $\langle \boldsymbol{\epsilon} \boldsymbol{\epsilon}^\dagger \rangle$ is the noise covariance of the radial velocities. Note that the lowercase bold letters indicate the vector quantity.

The sample covariance matrices were computed over 5000 realizations, which contain most of the variability in the observed vector current fields. The vector current maps estimated from the objective mapping of the sample covariance matrices do not agree well with the true vector current maps (Figs. A2e and A2f) because cov_{dm} and cov_{dd} do not contain sufficient information of the true vector current fields [Eq. (2)].

APPENDIX B

LSF-Mapped Vector Current Components under a Reduced Search Radius

In a similar way presented in Figs. 1c–f, 3–6, the estimated vector current components and the corresponding uncertainty, and their ensemble average of the estimated u component using LSF under a reduced search radius ($\beta_a = 1.5$ km) are evaluated to avoid oversampling the data field and minimizing spatial smoothing (Figs. B1–B3). The current components estimated under a shorter search radius are more similar to the true values and their uncertainty is relatively higher than the estimated data under a longer search radius ($\beta_a = 4$ km; Figs. 1c–f and B1).

The ensemble-averaged uncertainty has a minimum in the middle of the domain and significantly increases as it gets near the baseline or onshore (Fig. B2). The ensemble-averaged misfit fluctuates dominantly regardless of gridding locations and values of the chosen parameters (Fig. B3) except for the cases to simulate variation of the missing data and observational noise (Figs. B3e and B3f). The uncertainty is nearly constant regardless of the noise level (Fig. B2f).

APPENDIX C

Temporal Averaging of Radial Velocities

In a compact array system, a single radial velocity map is a set of radial solutions that are averaged over a time window between 1 and 3 h, depending on the length of the finite Fourier transform (FFT) in the internal calculation of the cross-spectra. For instance, a short-range system tends to yield hourly averaged radial velocity maps and a long-range system produces three-hourly averaged radial velocity maps. Conversely, a phased-array system generates radial velocity maps with a higher temporal resolution than 1 h, depending on the internal configuration. Thus, extracting a vector current map from radial velocity maps obtained from multifrequency radar systems should be addressed carefully

because more than two different types of temporal averaging are involved. In particular, it will be useful to investigate whether tidal amplitudes and phases of the vector currents contain biases and errors resulting from temporal averaging.

In this work the radial velocity maps obtained from a compact array system (e.g., SeaSonde CODAR) are discussed. There are multiple boxcar averages using a time window in the individual steps of data processing, and the center of the averaging time window is the time stamp in the operational system (Fig. C1). These multiple boxcar averages may cause the spread of pure signals (e.g., tides), which can appear as a time series having a reduced SNR (or increased noise level) or artificial nonlinear interactions (e.g., baroclinic tidal currents and near-inertial currents) (e.g., Brigham 1988). In a short-range radar system, for instance, a 10-min cross-spectra file is processed from the raw data (e.g., CSQ) within a 15-min-long time window, and an hourly radial solution is computed from an average of the cross-spectra files over a 60-min-long time window, that is, raw data within a 75-min-long time window (Fig. C1a). Similarly, an hourly radial solution in the long-range radar system is estimated from an average within a 60-min-long time window of the cross-spectra (equivalent to 180-min-long raw data), and each 30-min cross-spectra file is computed from the raw spectral data within a 60-min-long time window (Fig. C1b).

A sinusoidal time series with a pure M_2 tidal peak and white noise (e.g., 10% of the signal variance) for a period of 2 months is sampled and averaged as described above, and its energy spectra are compared. Although the noise level increases because of the multiple boxcar averages of the time series—that is, multiple time convolutions of a sinc function in the frequency domain—the location of the peak and the bandwidth obtained from temporal averaging simulations remains the same for both short- and long-range systems (Figs. C1c and C1d).

APPENDIX D

A Search Radius in OI

A search radius β_b in OI is proposed to minimize computational loads in the matrix inversion because the size of the covariance matrix depends on the number of participating radial velocities. The length scales at the lower bound of correlations ($\rho = \rho_0$) can be found as β_b^E and β_b^G for a one-dimensional exponential and Gaussian correlation functions, respectively (Fig. D1a). Similarly, the search radius can be found under a given lower bound of the correlation and the decorrelation length scale of the correlation function (Figs. D1b and D1c).

REFERENCES

- Barrick, D. E., 2002: Geometrical dilution of statistical accuracy (GDOSA) in multi-static HF radar networks. CODAR Ocean Sensors, Ltd., Tech. Manual, 9 pp., http://www.codar.com/Manuals/Informative/GDOSA_Definition.pdf.
- , 2003: Synthesis of total surface current vector maps by fitting normal modes to single-site HF radar data. U.S. Patent 6,590,523, filed 1 April 2002, and issued 8 July 2003.
- , M. W. Evans, and B. L. Weber, 1977: Ocean surface currents mapped by radar. *Science*, **198**, 138–144, <https://doi.org/10.1126/science.198.4313.138>.
- Bendat, J., and A. G. Piersol, 2000: *Random Data: Analysis and Measurement Procedures*. 3rd ed. John Wiley and Sons, 594 pp.
- Bjorkstedt, E., and J. Roughgarden, 1997: Larval transport and coastal upwelling: An application of HF radar in ecological research. *Oceanography*, **10** (2), 64–67, <https://doi.org/10.5670/oceanog.1997.25>.
- Bretherton, F. P., R. E. Davis, and C. B. Fandry, 1976: A technique for objective analysis and design of oceanographic experiment applied to MODE-73. *Deep-Sea Res. Oceanogr. Abstr.*, **23**, 559–582, [https://doi.org/10.1016/0011-7471\(76\)90001-2](https://doi.org/10.1016/0011-7471(76)90001-2).
- Brigham, E. O., 1988: *The Fast Fourier Transform and Its Applications*. Prentice Hall Signal Processing Series, Prentice-Hall, Inc., 448 pp.
- Chapman, R. D., L. K. Shay, H. Graber, J. B. Edson, A. Karachintsev, C. L. Trump, and D. B. Ross, 1997: On the accuracy of HF radar surface current measurements: Intercomparisons with ship-based sensors. *J. Geophys. Res.*, **102**, 18 737–18 748, <https://doi.org/10.1029/97JC00049>.
- Chavanne, C., I. Janeković, P. Flament, P.-M. Poulain, M. Kuzmić, and K.-W. Gurgel, 2007: Tidal currents in the northernwestern Adriatic: High-frequency radio observation and numerical model prediction. *J. Geophys. Res.*, **112**, C03S21, <https://doi.org/10.1029/2006JC003523>.
- Chelton, D. B., and M. G. Schlax, 1994: The resolution capability of an irregularly sampled dataset: With application to Geosat altimeter data. *J. Atmos. Oceanic Technol.*, **11**, 534–550, [https://doi.org/10.1175/1520-0426\(1994\)011<0534:TRCOAI>2.0.CO;2](https://doi.org/10.1175/1520-0426(1994)011<0534:TRCOAI>2.0.CO;2).
- , and —, 2003: The accuracies of smoothed sea surface height fields constructed from tandem satellite altimeter datasets. *J. Atmos. Oceanic Technol.*, **20**, 1276–1302, [https://doi.org/10.1175/1520-0426\(2003\)020<1276:TAOSSS>2.0.CO;2](https://doi.org/10.1175/1520-0426(2003)020<1276:TAOSSS>2.0.CO;2).
- Cohen, L., 1992: Convolution, filtering, linear systems, the Wiener-Khinchin theorem: Generalizations. *Advanced Signal Processing Algorithms, Architectures, and Implementations III*, F. T. Luk, Ed., Society of Photo-Optical Instrumentation Engineers, (SPIE Proceedings, Vol. 1770), 378–393, <https://doi.org/10.1117/12.130944>.
- Cook, T. M., and L. K. Shay, 2002: Surface M₂ tidal currents along the North Carolina shelf observed with a high-frequency radar. *J. Geophys. Res.*, **107**, 3222, <https://doi.org/10.1029/2002JC001320>.
- Cosoli, S., and G. Bolzon, 2015: Accuracy of surface current mapping from high-frequency (HF) ocean radars. *Boll. Geofis. Teor. Appl.*, **56**, 55–70, <https://doi.org/10.4430/bgta0132>.
- Crombie, D. D., 1955: Doppler spectrum of sea echo at 13.56 Mc./s. *Nature*, **175**, 681–682, <https://doi.org/10.1038/175681a0>.
- Ducet, N., P.-Y. Le Traon, and G. Reverdin, 2000: Global high-resolution mapping of ocean circulation from TOPEX/Poseidon and ERS-1 and-2. *J. Geophys. Res.*, **105**, 19 477–19 498, <https://doi.org/10.1029/2000JC900063>.
- Emery, W. J., and R. E. Thomson, 1997: *Data Analysis Methods in Physical Oceanography*. Elsevier, 634 pp.
- Graber, H. C., B. K. Haus, R. D. Chapman, and L. K. Shay, 1997: HF radar comparisons with moored estimates of current speed and direction: Expected differences and implications. *J. Geophys. Res.*, **102**, 18 749–18 766, <https://doi.org/10.1029/97JC01190>.
- Greenslade, D. J., D. B. Chelton, and M. G. Schlax, 1997: The midlatitude resolution capability of sea level fields constructed from single and multiple satellite altimeter datasets. *J. Atmos. Oceanic Technol.*, **14**, 849–870, [https://doi.org/10.1175/1520-0426\(1997\)014<0849:TMRCOS>2.0.CO;2](https://doi.org/10.1175/1520-0426(1997)014<0849:TMRCOS>2.0.CO;2).
- Hickey, K. J., 2010: Method for measuring surface currents using a long-range single station high frequency ground wave radar system. U.S. Patent 7,690,250, filed 8 August 2008, and issued 6 April 2010.
- Kim, S. Y., 2010: Observations of submesoscale eddies using high-frequency radar-derived kinematic and dynamic quantities. *Cont. Shelf Res.*, **30**, 1639–1655, <https://doi.org/10.1016/j.csr.2010.06.011>.
- , 2015: Quality assessment techniques applied to surface radial velocity maps obtained from high-frequency radars. *J. Atmos. Oceanic Technol.*, **32**, 1915–1927, <https://doi.org/10.1175/JTECH-D-14-00207.1>.
- , E. J. Terrill, and B. D. Cornuelle, 2007: Objectively mapping HF radar-derived surface current data using measured and idealized data covariance matrices. *J. Geophys. Res.*, **112**, C06021, <https://doi.org/10.1029/2006JC003756>.
- , —, and —, 2008: Mapping surface currents from HF radar radial velocity measurements using optimal interpolation. *J. Geophys. Res.*, **113**, C10023, <https://doi.org/10.1029/2007JC004244>.
- , —, and —, 2009: Assessing coastal plumes in a region of multiple discharges: The U.S.–Mexico border. *Environ. Sci. Technol.*, **43**, 7450–7457, <https://doi.org/10.1021/es900775p>.
- , and Coauthors, 2011: Mapping the U.S. West Coast surface circulation: A multiyear analysis of high-frequency radar observations. *J. Geophys. Res.*, **116**, C03011, <https://doi.org/10.1029/2010JC006669>.
- , P. M. Kosro, and A. L. Kurapov, 2014: Evaluation of directly wind-coherent near-inertial surface currents off Oregon using a statistical parameterization and analytical and numerical models. *J. Geophys. Res. Oceans*, **119**, 6631–6654, <https://doi.org/10.1002/2014JC010115>.
- Kirincich, A., 2016: The occurrence, drivers, and implications of submesoscale eddies on the Martha's Vineyard inner shelf. *J. Phys. Oceanogr.*, **46**, 2645–2662, <https://doi.org/10.1175/JPO-D-15-0191.1>.
- Kundu, P. K., and I. M. Cohen, 2002: *Fluid Mechanics*. 2nd ed. Academic Press, 730 pp.
- Kuragano, T., Y. Fujii, and M. Kamachi, 2015: Evaluation of the Argo network using statistical space-time scales derived from satellite altimetry data. *J. Geophys. Res. Oceans*, **120**, 4534–4551, <https://doi.org/10.1002/2015JC010730>.
- Leben, R. R., G. H. Born, and B. R. Engbreth, 2002: Operational altimeter data processing for mesoscale monitoring. *Mar. Geod.*, **25**, 3–18, <https://doi.org/10.1080/014904102753516697>.
- Leeuwenburgh, O., and D. Stammer, 2002: Uncertainties in altimetry-based velocity estimates. *J. Geophys. Res.*, **107**, 3175, <https://doi.org/10.1029/2001JC000937>.
- Le Traon, P.-Y., F. Nadal, and N. Ducet, 1998: An improved mapping method of multisatellite altimeter data. *J. Atmos. Oceanic Technol.*, **15**, 522–534, [https://doi.org/10.1175/1520-0426\(1998\)015<0522:A1MMOM>2.0.CO;2](https://doi.org/10.1175/1520-0426(1998)015<0522:A1MMOM>2.0.CO;2).
- Levanon, N., 2000: Lowest GDOP in 2-D scenarios. *IEE Proc.*, **147**, 149–155, <https://doi.org/10.1049/ip-rsn:20000322>.

- Lipa, B. J., and D. E. Barrick, 1983: Least-squares methods for the extraction of surface currents from CODAR crossed-loop data: Application at ARSLOE. *IEEE J. Oceanic Eng.*, **8**, 226–253, <https://doi.org/10.1109/JOE.1983.1145578>.
- Liu, L., X. Wu, F. Cheng, S. Yang, and H. Ke, 2007: Algorithm for HF radar vector current measurements. *J. Oceanogr.*, **63**, 47–66, <https://doi.org/10.1007/s10872-007-0005-x>.
- O’Keefe, S., 2005: Observing the coastal ocean with HF radar. M.S. thesis, College of Oceanic and Atmospheric Sciences, Oregon State University, 117 pp., http://ir.library.oregonstate.edu/concern/graduate_thesis_or_dissertations/v405sd076.
- Paduan, J. D., and H. C. Graber, 1997: Introduction to high-frequency radar: Reality and myth. *Oceanography*, **10** (2), 36–39, <https://doi.org/10.5670/oceanog.1997.18>.
- , and L. Washburn, 2013: High-frequency radar observations of ocean surface currents. *Annu. Rev. Mar. Sci.*, **5**, 115–136, <https://doi.org/10.1146/annurev-marine-121211-172315>.
- Pierce, J. A., A. McKenzie, and R. H. Woodward, Eds, 1948: *LORAN, Long Range Navigation*. Vol. 4. McGraw-Hill Book Co., 476 pp.
- Prandle, D., 1991: A new view of near-shore dynamics based on observations from HF radar. *Prog. Oceanogr.*, **27**, 403–438, [https://doi.org/10.1016/0079-6611\(91\)90030-P](https://doi.org/10.1016/0079-6611(91)90030-P).
- Rogowski, P. A., E. Terrill, K. Schiff, and S. Y. Kim, 2015: An assessment of the transport of southern California stormwater ocean discharges. *Mar. Pollut. Bull.*, **90**, 135–142, <https://doi.org/10.1016/j.marpolbul.2014.11.004>.
- Schlax, M. G., and D. B. Chelton, 2003: The accuracies of crossover and parallel-track estimates of geostrophic velocity from TOPEX/Poseidon and Jason altimeter data. *J. Atmos. Oceanic Technol.*, **20**, 1196–1211, [https://doi.org/10.1175/1520-0426\(2003\)020<1196:TAOCAP>2.0.CO;2](https://doi.org/10.1175/1520-0426(2003)020<1196:TAOCAP>2.0.CO;2).
- Shay, L. K., J. Martinez-Pedraja, T. M. Cook, B. K. Haus, and R. H. Weisberg, 2007: High-frequency radar mapping of surface currents using WERA. *J. Atmos. Oceanic Technol.*, **24**, 484–503, <https://doi.org/10.1175/JTECH1985.1>.
- Stewart, R. H., 2006: *Introduction to Physical Oceanography*. Dept. of Oceanography, Texas A&M University, 354 pp.
- Ullman, D. S., J. O’Donnell, J. Kohut, T. Fake, and A. Allen, 2006: Trajectory prediction using HF radar surface currents: Monte Carlo simulations of prediction uncertainties. *J. Geophys. Res.*, **111**, C12005, <https://doi.org/10.1029/2006JC003715>.
- Voulgaris, G., N. Kumar, K.-W. Gurgel, J. C. Warner, and J. H. List, 2011: 2-D inner-shelf current observations from a single VHF Wellen Radar (WERA) station. *2011 IEEE/OES/CWTM Tenth Current, Waves and Turbulence Measurements (CWTM)*, J. Rizoli White and A. J. Williams III, IEEE, 57–65, <https://doi.org/10.1109/CWTM.2011.5759525>.
- Wells, D., and Coauthors, 1986: *Guide to GPS Positioning*. Canadian GPS Associates and University of New Brunswick, 601 pp., <https://doi.org/10.13140/2.1.3771.4889>.
- Wilkin, J. L., M. M. Bowen, and W. J. Emery, 2002: Mapping mesoscale currents by optimal interpolation of satellite radiometer and altimeter data. *Ocean Dyn.*, **52**, 95–103, <https://doi.org/10.1007/s10236-001-0011-2>.
- Wunsch, C., 1996: *The Ocean Circulation Inverse Problem*. Cambridge University Press, 442 pp.
- Yoo, J. G., S. Y. Kim, B. D. Cornuelle, A. L. Kurapov, and P. M. Kosro, 2017: A noninterpolated estimate of horizontal spatial covariance from nonorthogonally and irregularly sampled scalar velocities. *J. Atmos. Oceanic Technol.*, **34**, 2407–2430, <https://doi.org/10.1175/JTECH-D-17-0100.1>.